EVALUATING THE CAPABILITIES OF THE LATTICE BOLTZMANN METHOD FOR NON-NEWTONIAN AND FREE-SURFACE FLOW TOWARDS APPLICATIONS IN WELLBORE CEMENTING

by

Matthew Grasinger

BS in Civil Engineering, University of Pittsburgh, Pittsburgh, PA

2013

Submitted to the Graduate Faculty of

the Swanson School of Engineering in partial fulfillment

of the requirements for the degree of

Master of Science

University of Pittsburgh

2016

UNIVERSITY OF PITTSBURGH

SWANSON SCHOOL OF ENGINEERING

This thesis was presented

by

Matthew Grasinger

It was defended on

July 21, 2016

and approved by

John C. Brigham, PhD, Associate Professor, Department of Civil and Environmental Engineering

Julie M. Vandenbossche, PhD, Associate Professor, Department of Civil and Environmental Engineering

Anthony T. Iannacchione, PhD, Associate Professor, Department of Civil and Environmental Engineering

Thesis Advisor: John C. Brigham, PhD, Associate Professor, Department of Civil and Environmental Engineering

EVALUATING THE CAPABILITIES OF THE LATTICE BOLTZMANN METHOD FOR NON-NEWTONIAN AND FREE-SURFACE FLOW TOWARDS APPLICATIONS IN WELLBORE CEMENTING

Matthew Grasinger, M.S.

University of Pittsburgh, 2016

When oil and gas wellbores are drilled, barriers must be put in place to ensure that fluids do not leak out of the wellbore. Wellbore leakage can lead to environmental damage, loss of pressure at the wellhead, and consequently, loss of production. An important yet vulnerable barrier is the cement annulus. Every well has unique subsurface conditions, and so no cement slurry mix design both performs well and is economical for cementing all wells. The lattice Boltzmann method (LBM) is a promising technique for simulating primary wellbore cementing because it is well-suited for efficiently simulating non-Newtonian flows, multiphase multicomponent flows, and flows through complex geometries–namely, some of the complexities associated with the mechanics of primary cementing.

Despite the advantages of LBM, there are considerations that must be made, as with all computational methods, in regards to the accuracy and numerical stability of the solution. Issues with accuracy and numerical stability are especially relevant in the flow of non-Newtonian fluids because of the nonlinear constitutive relationship between shear stress and strain-rate. Chapter 1 is a numerical investigation of the accuracy, stability, and computational efficiency of different LB methods in simulating non-Newtonian fluid flow. The accuracy and computational time are presented in Section 1.4 for various LB methods applied to two different benchmark problems, Poiseuille flow and lid-driven cavity flow, with two different non-Newtonian constitutive models, the Bingham plastic constitutive relationship and a power-law constitutive relationship.

Once the ground-work has been laid for simulating non-Newtonian flows using LBM, the algorithm was extended in Chapter 2 to incorporate simulation of free-surface flow. The extended LBM model was used to study primary cementing of a dry annulus, i.e. an annulus that is not filled with drilling mud. More specifically, the study involved defining different cement slurry flows and investigating how well each slurry flow filled different wellbore geometries. The study is followed by conclusions and a discussion of future work.

TABLE OF CONTENTS

LIST OF TABLES

LIST OF FIGURES

PREFACE

I would like to thank my wife and best friend, Shelby, my parents, and my family. Their love, support, and example means everything to me. I would like to thank the best advisor ever, Dr. John Brigham, for his patience and for all that he has taught me. I would also like to thank the other members of my committee, Dr. Julie Vandenbossche, and Dr. Anthony Iannacchione, both of whom have been great guides and teachers to me. Lastly, I would like to thank my fellow students, especially Rob, Jing, Mo, and Scott, for helping me to learn along the way and for the comradery that every graduate student needs.

1.0 NUMERICAL INVESTIGATION OF THE ACCURACY, STABILITY, AND EFFICIENCY OF LATTICE BOLTZMANN MODELS IN SIMULATING NON-NEWTONIAN FLUID FLOW

1.1 ABSTRACT

The Lattice Boltzmann method (LBM) is a method based on computational statistical mechanics that is well-suited for complex flow such as non-Newtonian, free surface, and multiphase multicomponent flow. Non-Newtonian flow is the primary focus of this Chapter, as many practical engineering problems such as the flow of cement slurry and concrete, the filling of molds by molten metals and plastics, blood flow, etc., are best modeled as non-Newtonian fluids. LBM is typically applied to simulate flow through a series of time seps, each consisting of streaming particle distributions to neighboring nodes, and collisions of particle distributions at each node through a collision operator. The collision operator is of interest because it, along with the equilibrium distribution function, determine the physics that are simulated, e.g. constitutive laws, interfacial dynamics, etc., and it has implications on numerical stability and computational efficiency. In this Chapter, various collision operators and methods for stability enhancement were examined for their suitability for simulating non-Newtonian fluid flows in terms of accuracy, numerical stability and computational efficiency. The investigation was carried out as a numerical study looking for qualitative, yet practical, results; it included testing the BGK and MRT collision operators, with and without entropic filtering, as applied to Bingham plastics and power-law fluids. Two different benchmark problems were chosen for the flows: Poiseuille flow, and lid-driven square cavity flow. The test results are followed by recommendations for choice collision scheme given priority and problem type.

1.2 INTRODUCTION

The dynamic viscosity of a fluid is a measure of its resistance to shear deformation. For many fluids, at a constant temperature, the dynamic viscosity can be considered as constant. These fluids are known as Newtonian fluids. Non-Newtonian fluids have an apparent dynamic viscosity, or apparent resistance to shear stress, that is variable even at a constant temperature and is often a function of strain-rate. There are a number of fluids in science and engineering applications that can be classified as non-Newtonian: pastes, slurries, molten plastics, polymer solutions, dyes, varnishes, suspensions, and some biomedical liquids such as blood all behave in a non-Newtonian manner [2].

Of all of the different non-Newtonian behaviors that exist, there are two models under which much of the behaviors may be idealized: yield stress fluids and power-law fluids. Yield stress fluids, also known as Bingham plastics, do not flow until a threshold value of stress, referred to as its yield stress, is exceeded. Yield stress flow is relevant in many other disciplines and applications because of the many substances that exhibit yield stress behavior, e.g. pastes, paints, muds, molten plastics and metals, and in some cases, blood [3]. As a consequence, simulating yield stress fluids can help engineers develop better pastes and paints, understand the flow and deformation of mud and clay in geotechnical engineering, understand blood circulation, and better manufacture metal and plastic parts.

There other idealized non-Newtonian behavir, power-law behavior, is more commonly known as *shear-thinning*–when the apparent viscosity decreases with increasing strain-rate– or *shear-thickening*–when the apparent viscosity increases with increasing strain-rate. Shear-thinning fluids are also known as *pseudoplastics*, and some examples include polymer mixes and molten plastics. Shear-thickening fluids are also known as *dilatants*, and some examples include quicksand, a cornstarch and water mixture, and a silica and polyethylene glycol mixture.

Analytical solutions rarely exist for even the simplest non-Newtonian fluid flows because of the complexity that a nonlinear constitutive relationship entails. It is generally more practical to approximate the flow of non-Newtonian fluids using numerical methods. However, the nonlinear constitutive equation–typically of the form

$$\tau = \mu_{app}(\dot{\gamma})\dot{\gamma}, \tag{1.1}$$

where the apparent viscosity, μ_{app} is a function of the strain rate–results in certain challenges for numerical methods as well. Determining the apparent viscosity and strain-rate distribution of a flow over time will often require an iterative solution at every time step, a general Picard-type algorithm for such a process can be given as:

1. Start with initial guess for the apparent viscosity, $\mu_k = \mu_0$.
2. Solve for the flow using the current value of apparent viscosity, $\dot{\gamma}_k = \tau_k/\mu_k$.
3. Update the apparent viscosity, $\mu_{k+1} = \mu(\dot{\gamma}_k)$.
4. Return to Step 2 until convergence is met.

Numerical solutions work by discretizing the equations that govern the physics of interest. When the solution for fluid flow problems vary in space and time, a numerical approximation requires breaking the problem up into discrete locations and discrete time steps. The significance of approximating a solution by discretizing the governing equations is that the iterative solution for the constitutive equation must be solved at each discrete location for each discrete time step, which can become computationally expensive. The lattice Boltzmann method (LBM) is a numerical method for fluid flow that has the advantage that computing the strain rate is second-order accurate in space and local to each node [4]. This means that although an iterative solution is still required to determine the local strain rate and apparent viscosity, each iterative solution can be done in parallel, by a separate process, as they are independent of each other. Because hardware architectures have shifted from single, sequential processing systems to parallel processing systems, the local nature of the stress–strain-rate relationship in LBM gives it a distinct advantage for simulating non-Newtonian flow over some other numerical methods.

The lattice Boltzmann method has been studied and successively applied to modeling various flows of non-Newtonian fluids. For example, [5–10] developed LBM models for simulating yield stress flow. The LBM model results agreed well when compared to analytical solutions for Bingham plastic Poiseuille flow and values from literature for lid-driven cavity flow, which shows the feasibility of using LBM models for yield-stress fluids. LBM models for power-law fluid flow [3, 6, 11, 12], and blood flows using the K-L, Casson, and Carreau-Yasuda constitutive relationships [13], have also been successfully developed and verified.

LBM does however, have its drawbacks. LBM can be considered as a type of finite-difference scheme for the continuous Boltzmann equation, and as such, has numerical properties in common with finite-difference schemes. One such consideration associated with this view is the potential for numerical inaccuracies and instabilities [14–17]. Stability concerns are just as prevalent, if not more prevalent, in simulating non-Newtonian fluids because the nonlinear relationship between shear stress and strain-rate can lead to highly nonlinear fluctuations. Various schemes and strategies for incorporating the physics of non-Newtonian flow with LBM and yet maintaining a stable numerical method have been developed and studied. The simplest approach for simulating a shear-rate dependent viscosity, used in [5, 7, 8, 12, 18–20], is to make the collision frequency, which is proportional to apparent viscosity, variable and dependent on the local strain rate. A potential issue with the stability of the variable relaxation time approach is that as the collision frequency approaches 2 the viscosity approaches zero and overrelaxation occurs; and alternatively, if the relaxation time is much greater than one, the accuracy and stability of the method also degrades [21]. In order to ensure that the variable collision frequencies did not approach values leading to numerical instabilities, [18, 19, 22] set upper and lower bounds on allowable collision frequencies. Although bounding the collision frequency was shown to be effective in terms of stability, it is also nonphysical and can lead to approximations that are inaccurate, not because of round-off error or numerical instability, but because the collision does not reflect the proper constitutive relationship of interest. Another scheme for incorporating non-Newtonian effects into LBM is to use a constant collision frequency, typically unity, and to instead incorporate the local shear-rate effect through equilibrium distribution functions. This means particle distribution functions will always relax toward equilibrium at the same rate, but that the

definition of equilibrium is modified to represent the correct stress–strain-rate relationship. The equilibrium distribution function is derived for the specific constitutive relationship of interest using the Chapman-Enskog multiscale expansion. The equilibrium distribution functions for Bingham plastic fluids, and for power-law and Carreau fluids were derived, implemented, and verified in [10] and [23], respectively. The strategy of using an equilibrium distribution function that incorporates the local shear-rate effect has the advantage that, because the collision frequency is constant (at unity), the collision frequency will not approach zero, and will not result in overrelaxation, and the collision frequency will not reach values much greater than one, and so there is no reason to bound the collision frequency in a way that is nonphysical. [3] developed another constant-collision frequency LBM scheme for non-Newtonian flow by splitting the effects of constitutive relationship into Newtonian and non-Newtonian parts. The Newtonian part was modeled in the usual way, namely scaling the collision frequency to achieve the macroscopic (Newtonian) viscosity, and the non-Newtonian part was modeled as a source of momentum, i.e. as an external forcing term, that is dependent on local shear-rate. Although the constant-collision frequency strategies present interesting alternatives, the variable collision scheme is used in the present study because of its simplicity and generality, i.e. it can be easily fitted to any constitutive equation without for example, performing Chapman-Enskog multiscale expansion.

To improve upon the stability of LBM models, [24] developed a multiple-relaxation-time (MRT) collision operator, that takes place in moment space and allows each moment to relax at a different rate. [17] used von Neumann stability analysis to investigate the stability of the newly constructed LBM-MRT model and concluded LBM with the MRT collision operator was more stable, but with increased computational expense than the commonly used BGK collision operator. Note that although this increased computational expense was decided

to not be significant for Newtonian flows ($\approx$ 10-20% [17]), the issue may be magnified for non-Newtonian flow because an iterative solution for the constitutive equation can require that certain expensive computations be performed at each iteration (the strain rate tensor is determined from the nonequilibrium particle distribution which must be mapped into moment space when using the MRT collision operator). [8] concluded that the MRT collision operator was more stable for Bingham plastic flow and allowed the use of a more accurate approximation to the Bingham plastic constitutive relationship. However, what remains unclear is:

- What is the increased cost associated with the MRT collision operator when applied to non-Newtonian flow?
- Under what conditions, e.g. material parameters, physical problem, etc., for Bingham plastic fluid flow is the MRT collision operator necessary to maintain stability and/or accuracy?
- Under what conditions, e.g. material parameters, physical problem, etc, for power-law fluid flow is the MRT collision operator necessary to maintain stability and/or accuracy?
- What are additional strategies for increasing stability and accuracy, and what are their associated computational costs?

In regards to the last question, much work has been done recently to enhance stability of LBM models beyond the MRT collision operator. [25–29] have all developed and tested means for introducing artificial dissipation in order to dampen out high frequency, nonphysical oscillations. Stability enhancement through artificial dissipation and entropic filtering has shown a lot of promise, but to the authors' knowledge has not been tested for use in simulating the flow of non-Newtonian fluids.

The goal of this Chapter is to numerically study the implications of accuracy, stability, and efficiency for some of the different strategies for simulating non-Newtonian flow using LBM. The intention of the study is to aid scientists and engineers in understanding which strategy is best suited to their priorities and applications of interest so as to maximize the advantages LBM has in simulating non-Newtonian flow. Advantages, such as LBM's potential to scale well in parallel, can be much less realized if the collision operator is too

computationally expensive, or if numerical instabilities ensue. A numerical study can help to determine approximate numerical values, domains, and boundary conditions in which one LBM scheme may be more advantageous than another so that LBM may be used in a computationally efficient and stable manner.

1.3 LATTICE BOLTZMANN METHOD FOR SIMULATION OF NON-NEWTONIAN FLUIDS

The Lattice Boltzmann method is a numerical approach that uses statistical mechanics to represent a variety of physical processes, such as fluid flow. More specifically, LBM can be thought of as a special finite difference discretization of the Boltzmann equation [30]. The length scale of LBM is unique in contrast to most common numerical methods, and is referred to as the mesoscale. In contrast to continuum based methods, LBM simulates the kinetics of microscopic particles, and so it reaches a finer length scale than the macroscopic domain of continuum mechanics; and in contrast to molecular dynamics, discrete element method, and other particle scale approaches, LBM does not deal with a complete description of the degrees of freedom for each individual particle. LBM instead relies on a statistical description of particle distributions, making LBM, in general, more computationally efficient and requiring less memory than other particle methods. Thus, LBM can be seen as a compromise between continuum and particle methods, combining strengths from each.

LBM has some advantages over other methods of CFD. For example, LBM is a computationally efficient approach for some CFD. This efficiency is a consequence of two distinct features of LBM: (1) the convective operator is linear, as opposed to the nonlinear convection terms that appear in continuum mechanics approaches; and (2) the fluid pressure is given by an equation of state. Solving for the fluid pressure in traditional method is more computationally expensive and requires special treatment such as iteration and/or relaxation [30].

1.3.1 The Boltzmann Equation

The Boltzmann equation (BE) can be thought of as a conservation of particle distributions. The BE is given as:

$$\frac{\partial f}{\partial t} + \boldsymbol{\xi} \cdot \boldsymbol{\nabla} f = \Omega, \tag{1.2}$$

where $f = f(\mathbf{x}, \boldsymbol{\xi}, t)$ is the particle velocity distribution function, $\mathbf{x}$ is the spatial position vector, $\boldsymbol{\xi}$ is the particle velocity, and $\Omega = \Omega(f)$ is the collision operator. The lattice part of LBM refers to the way in which the BE is discretized. The lattice discretizes the spatial domain with nodes that are connected to their neighbors through discrete lattice velocity vectors. The velocity vectors act as pathways for particle distributions to travel along. Each time step in LBM consists of two distinct actions:

- Streaming: particle distributions propagate to their neighbors along the lattice velocity vectors. The particles can only move along the vectors in their specified direction and can only move at a specific speed.

- Collision: particle distributions meet at a node and "collide". In LBM, collisions are not simulated in a realistic sense, meaning that each individual particle does not exist and glance off of, or interact with, one another. Instead the collision operator is formulated in such a way that particle distributions are relaxed toward equilibrium. What defines equilibrium depends on the mechanics of interest to be modeled.

The D2Q9 lattice was used in the current work (shown in Figure 1.1), which is commonly used for two-dimensional, incompressible flow simulations [31]. The lattice is two-dimensional with nine discrete velocities at each node. There is a stationary particle, there are four discrete velocities of magnitude 1, $\begin{Bmatrix} 1 & 0 \end{Bmatrix}^T$, $\begin{Bmatrix} 0 & 1 \end{Bmatrix}^T$, $\begin{Bmatrix} -1 & 0 \end{Bmatrix}^T$, $\begin{Bmatrix} 0 & -1 \end{Bmatrix}^T$, and there are four discrete velocities of magnitude $\sqrt{2}$, $\begin{Bmatrix} 1 & 1 \end{Bmatrix}^T$, $\begin{Bmatrix} -1 & 1 \end{Bmatrix}^T$, $\begin{Bmatrix} -1 & -1 \end{Bmatrix}^T$, $\begin{Bmatrix} 1 & -1 \end{Bmatrix}^T$. The discretized version of the Boltzmann equation, or the lattice Boltzmann equation (LBE), is given as:

$$f_i(\mathbf{x} + \boldsymbol{\xi}_i \Delta t, t + \Delta t) = f_i(\mathbf{x}, t) + \Omega_i(\mathbf{x}, t), \tag{1.3}$$

where, for D2Q9, $i = 0, 1, ..., 8$ is the index of the discrete velocity vector.

The macroscopic variables of interest can be calculated from the particle distribution functions, $f(\mathbf{x}, \boldsymbol{\xi}, t)$, by integrating moments of f over velocity space. Due to the discrete nature of velocity in LBM, the integrals simply become summations. The mass density is given by the sum of the particle distributions and the momentum density is given by the first moment of the particle distributions over the velocity space:

$$\rho(\mathbf{x}, t) = \sum_i f_i(\mathbf{x}, t), \tag{1.4}$$

$$\mathbf{j}(\mathbf{x}, t) = \rho(\mathbf{x}, t)\mathbf{u}(\mathbf{x}, t) = \sum_i \boldsymbol{\xi}_i f_i(\mathbf{x}, t) \tag{1.5}$$

The fluid pressure is related to macroscopic density through an equation of state:

$$p(\mathbf{x}, t) = \rho(\mathbf{x}, t) c_s^2, \tag{1.6}$$

where c_s is the lattice speed of sound ($c_s = \frac{1}{\sqrt{3}}$, for D2Q9).

1.3.2 Collision Operator

1.3.2.1 Bhatnagar-Gross-Krook (BGK) The collision operator, in the case of the continuous BE, attempts to describe the change in particle momentums and trajectories due to pairwise particle collisions (based on their respective momentums and trajectories just prior to collision) [32]. In LBM, the collision operator causes particle distributions

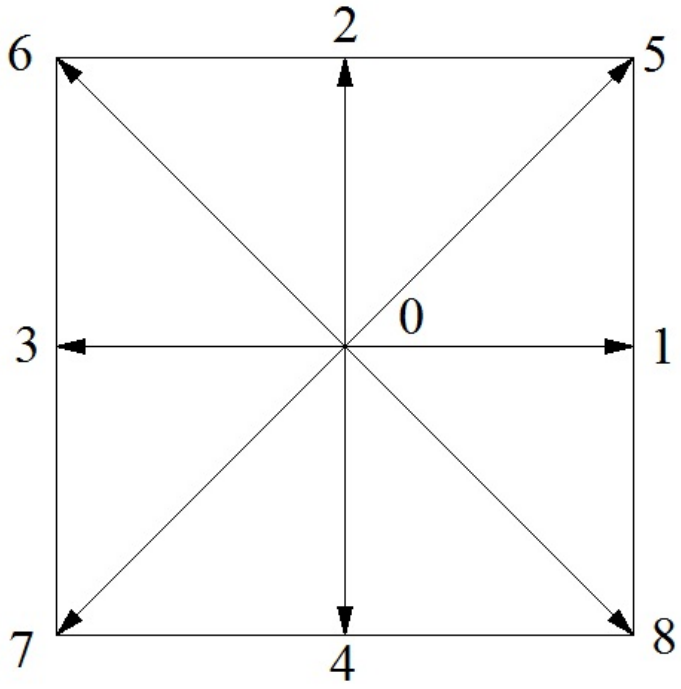

Figure 1.1: Schematic of D2Q9 lattice, each node is connected to its neighbor by one of eight discrete velocity vectors

to relax toward a quasiequilibrium. This equilibrium is determined by the macroscopic physical behavior of interest. In the case of incompressible flow, the quasiequilibrium particle distribution, $f_i^{eq} = f_i^{eq}(\mathbf{x}, t)$, is often given by:

$$f_i^{eq} = w_i \rho \left[1 + \frac{\boldsymbol{\xi}_i \cdot \mathbf{u}}{c_s^2} + \frac{(\boldsymbol{\xi}_i \cdot \mathbf{u})^2}{4c_s^2} - \frac{\mathbf{u}^2}{2c_s^2} \right], \tag{1.7}$$

where ρ and $\mathbf{u}$ are dependent on $\mathbf{x}$ and t, and w_i is the weight in the i^{th}:

$$w_i = \begin{cases} \frac{4}{9}, & i = 0 \\ \frac{1}{9}, & i = 1, 2, 3, 4 \\ \frac{1}{36}, & i = 5, 6, 7, 8 \end{cases}. \tag{1.8}$$

Due to its simplicity and computational efficiency, the most common collision operator is the Bhatnagar–Gross–Krook (BGK) operator. BGK consists of a single relaxation time and is a linear relaxation of particle distributions toward equilibrium. The BGK collison operator for the i^{th} discrete velocity is expressed as:

$$\Omega_i(\mathbf{x}, t) = -\omega(f_i(\mathbf{x}, t) - f_i^{eq}(\mathbf{x}, t)), \tag{1.9}$$

where ω is the collision frequency [33]. The collision frequency can be related to macroscopic constitutive properties through Chapman-Enskog multiscale analysis [34]. For incompressible Newtonian flow, the collision frequency is related to the kinematic viscosity by $\nu = c_s^2(\frac{1}{\omega} - \frac{1}{2})$; and from this relationship it is clear that $\omega \in [0.0, 2.0]$, otherwise the viscosity would be negative. The method for simulating non-Newtonian flow in the current work involves approximating a solution to the local value of apparent viscosity, $\mu_{app}(\mathbf{x}, t)$, using (1.1) where τ and $\dot{\gamma}$ are dependent on $\mathbf{x}$ and t, and then setting the value of the local collision frequency as follows:

$$\omega(\mathbf{x}, t) = \frac{1}{\frac{\mu_{app}(\mathbf{x},t)}{c_s^2 \rho(\mathbf{x},t)} + \frac{1}{2}} \tag{1.10}$$

Despite the utility of the BGK collision operator, it does have a few drawbacks. For example, in low viscosity fluids the BGK operator results in an overrelaxation of particle distributions toward quasiequilibrium. It is well known that when large nonequilibrium distributions exist in the LBM approximation that overrelaxation can result in nonphysical

oscillations that are slow to decay [26, 35]. To illustrate this, consider a flow in which there is a sharp spatial gradient in either ρ or $\mathbf{u}$ at $\mathbf{x}$. As f_i^{eq} depends on both ρ and $\mathbf{u}$ (1.7), it may be the case that $|f_i^{eq}(\mathbf{x},t) - f_i^{eq}(\mathbf{x}+\boldsymbol{\xi}_i\Delta t, t+\Delta t)| >> 0$, i.e. there may be a large difference in the quasiequilibrium for the i^{th} discrete velocity at $(\mathbf{x},t)$ and $(\mathbf{x}+\boldsymbol{\xi}_i\Delta t, t+\Delta t)$. In this case, if f_i is "near" to quasiequilibrium at $\mathbf{x}$ it will be "far" from quasiequilibrium after the streaming step when it moves to the node at $\mathbf{x}+\boldsymbol{\xi}_i\Delta t$. Overrelaxation will occur if $\nu \to 0$ because consquently $\omega \to 2$ and (1.9) results in $f_i(\mathbf{x}+\boldsymbol{\xi}_i\Delta t, t+\Delta t)$ still being "far" from $f_i^{eq}(\mathbf{x}+\boldsymbol{\xi}_i\Delta t, t+\Delta t)$ but on the "other side". Overrelaxation in subsequent time steps (along the streaming trajectory of f_i) could result in nonphysical oscillations such as those depicted in Figure 1.2. Considering the effect oscillations of particle distributions will have on macroscopic variables and, consequently, local quasiequilibriums, positive feedback loops can occur causing the system to diverge or "pollute" the system enough to make the results highly nonphysical and altogether useless [29].

The challenge associated with high viscosity fluids is that particular distributions may never relax as "far" toward quasiequilibrium as is physical because $\omega \to 0$ as $\nu \to \infty$, resulting in extreme underrelaxation to the point of being negligible.

Concerns with sharp gradients, overrelaxation, and underrelaxation are particularly relevant in non-Newtonian flow because of the nonlinear constitutive relationship between shear stress and strain-rate. The nonlinear constitutive relationship can lead to sharp gradients in ρ or $\mathbf{u}$, and depending on the form of the function $\mu_{app}(\dot{\gamma})$, the apparent viscosity, $\mu(\dot{\gamma}(\mathbf{x}))$, may result in overrelaxation in certain parts of the domain and extreme underrelaxation in others.

Due to the instabilities associated with the collision frequency being too high (e.g. approaching 2) or too low (e.g. approaching 0), a natural, albiet nonphysical, approach to using the BGK collision operator for non-Newtonian flow is to simply put bounds on the values in which the collision frequency may attain (such as in [18, 19, 22]). This simple methodology for increasing stability will henceforth be referred to bounded-relaxation time BGK, or BGK-BRT.

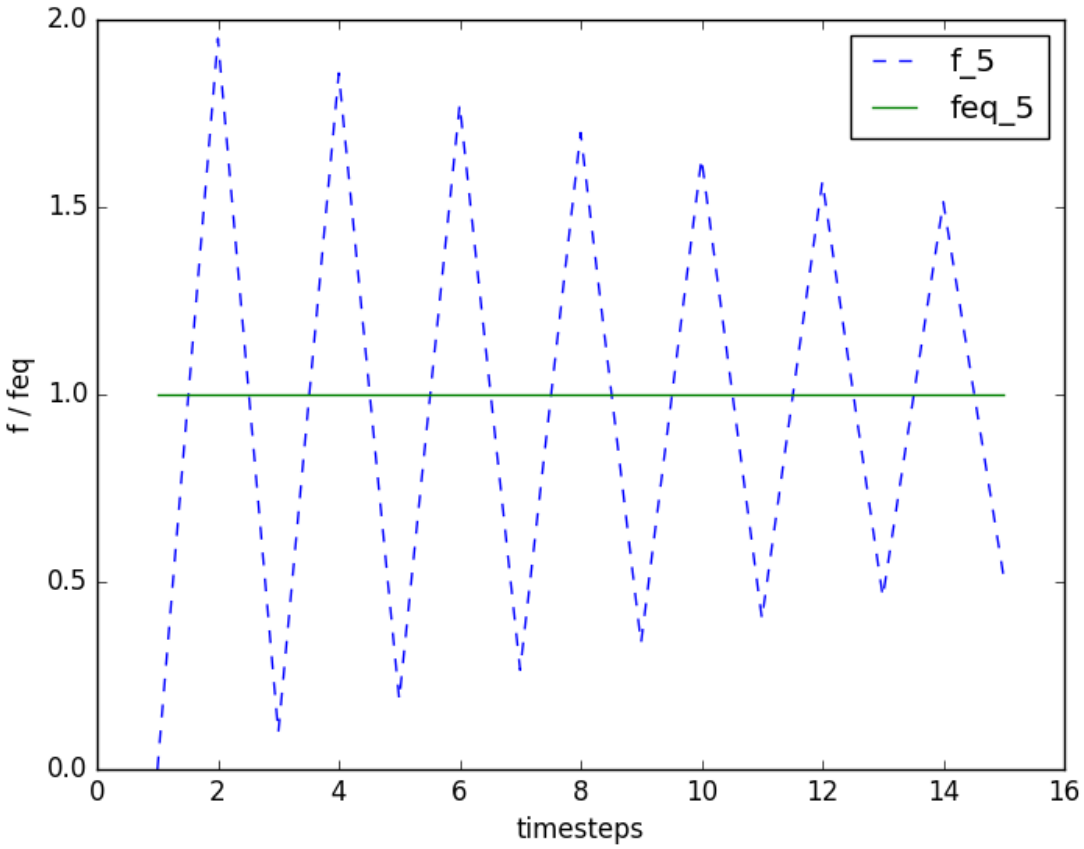

Figure 1.2: Example of oscillations that can occur as a result of overrelaxation; the collision frequency, $\omega = 1.95$ and $\mu_{app} \approx 0.0043$

1.3.2.2 Multiple-relaxation Time (MRT) An alternative to the BGK collision operator is the multiple-relaxation-time (MRT) collision operator. In the LB-MRT scheme, one constructs a space based on the particle velocity, $\boldsymbol{\xi}$, moments of $\mathbf{f} = \begin{Bmatrix} f_0 & f_1 & ... & f_8 \end{Bmatrix}$, herein referred to as the "moment space". The collision is then performed in the moment space. There are a few reasons why it is advantageous to perform the collision in the moment space as opposed to the particle distribution space:

1. Physical processes in fluids can be approximately described by coupling or interacting among modes, and the modes are directly related to the moments [17].
2. For the D2Q9 lattice, there are nine distribution functions, $f_0, f_1, ..., f_8$, but only six variables that affect the intended hydrodynamics on a macroscopic scale, namely: ρ, $\mathbf{u}$, and $\mathbf{\Pi}$, where $\mathbf{\Pi}$ is the momentum flux tensor [35]. Of the nine relaxation rates available, the three that correspond to the extra variables–often referred to as "ghost variables", and their associated modes as "ghost modes"–can be tuned in order to dampen out their associated ghost modes, ensuring these modes do not dominate or cause numerical instabilities at the lattice scale.

   The MRT collision operator is given by:

$$\Omega = -\mathbf{M}^{-1}\mathbf{S}\mathbf{M}(\mathbf{f} - \mathbf{f}^{eq}), \tag{1.11}$$

where $\mathbf{M}$ is a transformation matrix that maps the particle distribution vector, $\mathbf{f}$, and quasiequilibrium distribution vector, $\mathbf{f}^{eq}$, from the particle distribution space into moment space. The result of mapping the vectors $\mathbf{f}$ and $\mathbf{f}^{eq}$ into moment space will be denoted by $\mathbf{m}$ and $\mathbf{m}^{eq}$, respectively. The relationships between $\mathbf{m}$, $\mathbf{M}$ and $\mathbf{f}$ can be written as follows:

$$\mathbf{m} = \begin{bmatrix} \rho \\ e \\ \epsilon \\ j_x \\ q_x \\ j_y \\ q_y \\ p_{xx} \\ p_{xy} \end{bmatrix} = \begin{bmatrix} 1 & 1 & 1 & 1 & 1 & 1 & 1 & 1 & 1 \\ -4 & -1 & -1 & -1 & -1 & 2 & 2 & 2 & 2 \\ 4 & -2 & -2 & -2 & -2 & 1 & 1 & 1 & 1 \\ 0 & 1 & 0 & -1 & 0 & 1 & -1 & -1 & 1 \\ 0 & -2 & 0 & 2 & 0 & 1 & -1 & -1 & 1 \\ 0 & 0 & 1 & 0 & -1 & 1 & 1 & -1 & -1 \\ 0 & 0 & -2 & 0 & 2 & 1 & 1 & -1 & -1 \\ 0 & 1 & -1 & 1 & -1 & 0 & 0 & 0 & 0 \\ 0 & 0 & 0 & 0 & 0 & 1 & -1 & 1 & -1 \end{bmatrix} \begin{bmatrix} f_0 \\ f_1 \\ f_2 \\ f_3 \\ f_4 \\ f_5 \\ f_6 \\ f_7 \\ f_8 \end{bmatrix} = \mathbf{M}\mathbf{f}. \tag{1.12}$$

where ϵ is related to the square of the energy e; q_x and q_y correspond to the energy fluxes in the x and y directions; and p_{xx} and p_{xy} correspond to the diagonal and off-diagonal component of the viscous stress tensor [17]. The relaxation matrix, $\mathbf{S}$, is a diagonal matrix where each

of the elements on the diagonal, $s_i \in [0, 2], i = 0, 1, ..., 8$, correspond to the relaxation rate of its associated hydrodynamic mode. In the case when $s_0 = s_1 = ... = s_8 = \omega$ (ω is the collision frequency in the BGK sense), the MRT collision operator is equivalent to the BGK collision operator. The relaxation parameters s_0, s_3, and s_5 are all set to zero as mass and momentum should be conserved. The relaxation parameters s_1 and $s_7 = s_8$ are related to the bulk and shear viscosities, respectively. The relationship for the shear viscosity is given by:

$$\nu = c_s^2 \Delta t (\frac{1}{s_7} - \frac{1}{2}), \tag{1.13}$$

which is equivalent with the relationship to the collision frequency, ω, in the BGK sense (when $\Delta t = 1$). The remaining relaxation parameters, s_2, s_4, and s_6, are tuned in order to dampen out and separate the ghost modes from the modes affecting hydrodynamic transport. It is common practice, and [17] recommends, that these three relaxation parameters be set to slightly larger than one.

The MRT collision operator has a greater numerical stability than its BGK counterpart [17, 35, 36], and because of the challenges associated with simulating non-Newtonian flow, the MRT collision operator has become popular for simulating non-Newtonian fluids [5–9, 37]. The main drawback of the MRT collision operator is its computational expense. Why MRT is more computationally expensive is clear when one considers that (1.11) requires multiple matrix multiplications and (1.9) requires none. It has been reported that MRT is approximately 15% slower than BGK [36], but this was in the context of Newtonian flow. As will be shown later, for certain LBM implementations and non-Newtonian fluid flows the increase in computational expense can be much greater.

1.3.3 Stability Enhancement through Artificial Dissipation: Entropic Filtering

To reduce nonequilibrium fluctuations in LBM, one can introduce artificial dissipation. The idea of artificial dissipation is to increase numerical stability, while sacrificing some physical accuracy. A model that has more physical justification but produces unstable and nonsensical results is much less useful than a model with some minor artificial features yet produces more stable results. A practical goal then would be to use only the necessary amount of artificial

dissipation in order to ensure a stable solution. From this goal two questions naturally arise: "under what criteria does one decide that artificial dissipation is necessary?" and "how much artificial dissipation does one introduce when it is necessary?".

To answer the first question, consider the discussion in Section 1.3.2.1 on problems with overrelaxation and nonphysical oscillations. Nonphysical oscillations due to overrelaxation would be damped out more quickly if particle distributions "far" from quasiequilibrium were brought closer to quasiequilibrium. A particle distribution vector, $\mathbf{f}$, "far" from equilibrium would be a good candidate for artificial dissipation. There are many ways one can measure the distance between $\mathbf{f}$ and $\mathbf{f}^{eq}$; for example, a reasonable choice would be $||\mathbf{f} - \mathbf{f}^{eq}||_p$ for some p norm. A metric that has been developed and used successfully for determining when artificial dissipation should be introduced at a lattice site is the so called relative nonequilibrium entropy [25–29]. The relative nonequilibrium entropy, ΔS, is given by:

$$\Delta S = \sum_i f_i \ln(\frac{f_i}{f_i^{eq}}). \tag{1.14}$$

A more computationally efficient approximation of ΔS can be achieved by instead using the second order Taylor expansion of (1.14):

$$\Delta S \approx \sum_i \frac{(f_i - f_i^{eq})^2}{2 f_i^{eq}}. \tag{1.15}$$

Note that limiting nonequilibrium entropy in LBM is analogous to what flux limiters do in finite difference, finite volume, and finite element methods [27].

A criteria for introducing artificial dissipation that has been used successfully [25–27, 29] is to define a threshold, θ, such that dissipation is added when:

$$\Delta S(\mathbf{x}, t) > \theta. \tag{1.16}$$

A potential drawback of defining a threshold *a priori* is that in order to ensure the model still retains some physical integrity, only a small number of sites can have artificial dissipation added. If the threshold is too low, too many sites may have dissipation added. If the threshold

is too high, a stable solution may not be achieved. The threshold can be determined on a case-by-case basis through trial-and-error or by a preliminary analysis. In the current work, the criteria that is used for determining whether dissipation should be added is a combination of (1.16) and the following:

$$\Delta S(\mathbf{x}, t) > \overline{\Delta S} + n_\sigma \cdot \sigma_{\Delta S}, \tag{1.17}$$

where $\overline{\Delta S}$ and $\sigma_{\Delta S}$ are the mean and standard deviation of ΔS, respectively–both are calculated using values over the domain for the current timestep–and n_σ is the number of standard deviations greater than $\overline{\Delta S}$ that ΔS must be before dissipation is added. The number of standard deviations, n_σ, is chosen *a priori*. The criteria described in (1.17) has the advantage that one does not need to determine *a priori* what constitutes "far" from quasiequilibrium, but instead can think in terms of what would be the maximum percentage of sites one would want artificial dissipation to be added to. A disadvantage of (1.17) is that if $\overline{\Delta S}$ and n_σ are both small then it is possible for dissipation to be added when $\Delta S(\mathbf{x}, t)$ is low and artifical dissipation is unnecessary. By required that both (1.16) and (1.17) be met before artifical dissipation is added, there is the potential for (1.16) and (1.17) to compensate for the each other's disadvantage.

Just as there are many ways to measure a lattice site's distance from quasiequilibrium, or from that measure define criteria for artificial dissipation, there are also many different ways of deciding how much dissipation to add. One method of adding dissipation is the so-called Ehrenfests' regularization [25], and involves setting a lattice site that is chosen for artificial dissipation to its quasiequilibrium state. Although this achieves the desired result, namely damping out large nonequilibrium fluctuations, it does so in a way that is not smooth or gradual, but sharp. An alternative, the median filter, has been used successfully in conjunction with both the BGK and MRT collision schemes for simulating one-dimensional shock tubes and lid-driven cavity flow [27–29]. Median filtering is an effective noise reduction technique, often used in image processing, for "speckle noise" or "salt and pepper noise" [27]. In other words, median filters are good at reducing high frequency noise while having a minimal effect on lower frequency noise. In LBM this is a desirable way to introduce dissipation because it has the potential to reduce high frequency nonequilibrium

fluctuations that might lead to numerical instability while retaining the lower frequency dynamics. To use the median filter one performs the collision step and then checks over the domain for lattice sites with ΔS that meet the criteria for artificial dissipation; sites that meet the criteria are updated as follows:

$$\mathbf{f} = \mathbf{f}^{eq} + \delta(\mathbf{f} - \mathbf{f}^{eq}), \tag{1.18}$$

where $\delta = \sqrt{\Delta S_{med}/\Delta S}$ is the scaling coefficient, and ΔS_{med} is the median value of ΔS for the nearest neighbors of the lattice site.

1.3.4 Boundary Conditions

No slip, or zero velocity, which is commonly imposed at walls in a domain, is accomplished by simulating the particle distributions as "bouncing back" at the walls in the opposite direction from which they stream. For example, for a particle distribution streaming in the direction of a south wall, $f_2 = f_4$, $f_5 = f_7$, and $f_6 = f_8$. For velocity or pressure boundary conditions, the method proposed by [38] can be used. The particle distributions that are missing after the streaming step are solved for by assuming a bounceback of the nonequilibrium distribution in the direction normal to the boundary; e.g., for a south inlet or outlet, $f_2 - f_2^{eq} = f_4 - f_4^{eq}$.

1.3.5 Applied Forces

Incorporating external forces, such as gravity, pressure gradients, etc., is done by adding a source of particle distributions in the direction of the force. The increase in particle distributions leads to the desired macroscopic result–an increase in momentum. The LBE with external forces is:

$$f_i(\mathbf{x} + \boldsymbol{\xi}_i \Delta t, t + \Delta t) = f_i(\mathbf{x}, t) + \Omega_i(f) + \frac{w_i \Delta t}{c_s^2} \mathbf{F} \cdot \boldsymbol{\xi}_i \tag{1.19}$$

where $\mathbf{F}$ is the body force vector.

1.3.6 Strain-rate Tensor

In order to solve for the apparent viscosity, μ_{app}, using the Picard-type algorithm outlined in Section 1.2, one must calculate the strain-rate, $\dot{\gamma}$. The strain-rate is given by the second invariant of the strain-rate tensor, $D_{\alpha\beta}$, i.e.:

$$\dot{\gamma} = \sqrt{2 \sum_{\alpha,\beta=1}^{2} D_{\alpha\beta} D_{\alpha\beta}}. \tag{1.20}$$

When using the BGK collision scheme, the strain-rate tensor is determined by:

$$D_{\alpha\beta} = -\frac{\omega}{2\rho c_s^2} \sum_i \xi_{i\alpha} \xi_{i\beta} (f_i - f_i^{eq}), \tag{1.21}$$

and for the MRT collision scheme, the strain-rate tensor is determined by:

$$D_{\alpha\beta} = -\frac{1}{2\rho c_s^2 \Delta t} \sum_i \xi_{i\alpha} \xi_{i\beta} \sum_j (\mathbf{M}^{-1}\mathbf{S}\mathbf{M})_{ij} (f_i - f_i^{eq}). \tag{1.22}$$

Computing the strain-rate tensor by either (1.21) or (1.22) is second order accurate in space [4, 39].

Upon comparison of (1.21) and (1.22), it is clear that calculating the strain-rate tensor for the MRT collision operator is more computationally expensive than it is for the BGK collision operator. The increase in computational expense is exacerbated by the fact that approximating the apparent viscosity, μ_{app}, by the algorithm outlined in Section 1.2 requires iteration and therefore multiple calculations of the strain-rate tensor.

1.3.7 Non-Newtonian Constitutive Equations

1.3.7.1 Bingham Plastic The Bingham plastic constitutive model is popular for yield stress flow. A Bingham plastic does not flow, i.e. the strain-rate is zero, when the shear stress is below the yield stress, and behaves in an almost Newtonian manner when the shear stress is above the yield stress. The Bingham plastic relationship is described mathematically as:

$$\begin{cases} \tau = \tau_y + \mu_p \dot{\gamma}, & |\tau| \geq \tau_y \\ \dot{\gamma} = 0, & |\tau| < \tau_y \end{cases} \tag{1.23}$$

where τ is the shear stress, τ_y is the yield stress, and μ_p is the plastic viscosity [40].

Due to the discontinuous nature of (1.23), the Bingham plastic model is difficult to work with numerically. Thus, a smooth approximation to (1.23) formulated by [41] is often used as:

$$\tau = \tau_y(1 - e^{-m|\dot{\gamma}|}) + \mu_p \dot{\gamma}, \tag{1.24}$$

where m is the stress growth exponent. The larger the value of m, the closer the approximation is to the Bingham plastic model.

Alternatively, the constitutive relationship can be interpreted through the apparent viscosity. Noting that $\mu_{app} = \frac{\tau}{\dot{\gamma}}$ and rearranging (1.24) results in the following expression for the apparent viscosity:

$$\mu_{app} = \frac{\tau_y}{\dot{\gamma}}(1 - e^{-m|\dot{\gamma}|}) + \mu_p. \tag{1.25}$$

1.3.7.2 Power-law The power-law constitutive relationship is useful for modeling fluids that experience shear-thinning or shear-thickening. The power-law relationship is given by:

$$\tau = k\dot{\gamma}^n, \tag{1.26}$$

where k is the flow consistency index and n is the flow behavior index. When $n = 1$, (1.26) results in a Newtonian constitutive relationship with dynamic viscosity, $\mu = k$. A flow consistency index of $n < 1$ results in shear-thinning behavior, where as $n > 1$ results in shear-thickening. As with the Bingham plastic relationship, (1.26) can be modified to determine an apparent viscosity:

$$\mu_{app} = k\dot{\gamma}^{n-1}. \tag{1.27}$$

1.4 NUMERICAL STUDY

A numerical study was carried out in order to investigate the suitability of different LBM collision schemes for simulating non-Newtonian flow in terms of accuracy, numerical stability and computational efficiency. For all simulations presented in this section, the apparent viscosity is approximated using its corresponding constitutive relationship and the Picard-type algorithm outlined in Section 1.2 with the maximum number of iterations set at 15 and the convergence criteria:

$$\frac{\left|\mu_{app}^{k+1} - \mu_{app}^{k}\right|}{\mu_{app}^{k}} < 1.0 \times 10^{-6}. \tag{1.28}$$

All BGK-BRT collision schemes use $\omega \in [0.05, 1.995]$ as the bounds on the collision frequency. All simulations with artificial dissipation use the median filter with $\theta = 1.0 \times 10^{-6}$ and $n_\sigma = 2.7$ where θ is the threshold that $\Delta S(\mathbf{x}, t$ must exceed before dissipation is added (1.16) and n_σ is the number of standard deviations greater than $\overline{\Delta S}$ that $\Delta S(\mathbf{x}, t)$ must be before dissipation is added (1.17). All numerical values given in this section are in lattice units unless otherwise stated.

1.4.1 Poiseuille Flow

Poiseuille flow is a useful benchmark because analytical solutions exist for both Bingham plastic and power-law fluids. Poiseuille flow is driven by a constant pressure gradient, $\frac{\partial p}{\partial x}$, through a two-dimensional channel. A schematic is shown in Figure 1.3. No-slip boundary conditions are enforced at the top and bottom boundaries with a wall velocity of zero so that $\mathbf{u} \times \hat{\mathbf{n}} = 0$ where $\hat{\mathbf{n}}$ is the unit normal vector to the boundary. Periodic boundary conditions are enforced at the left and right boundaries. The total height of the channel is denoted by H. The center of the channel is $y = 0$ and $y \in [-h, h]$ where $h = \frac{H}{2}$.

Unless otherwise stated, all of the Poiseuille flow simulations were computed on a 32×64 lattice for 25000 timesteps. The lattice size was chosen to be sufficiently fine for accuracy (although the length, $L = 32$, seems small, the effect is negligible as the east-west boundary conditions are periodic) and the number of time steps were set high enough to ensure a steady-state would be reached. In reference to computational time, each of the simulations

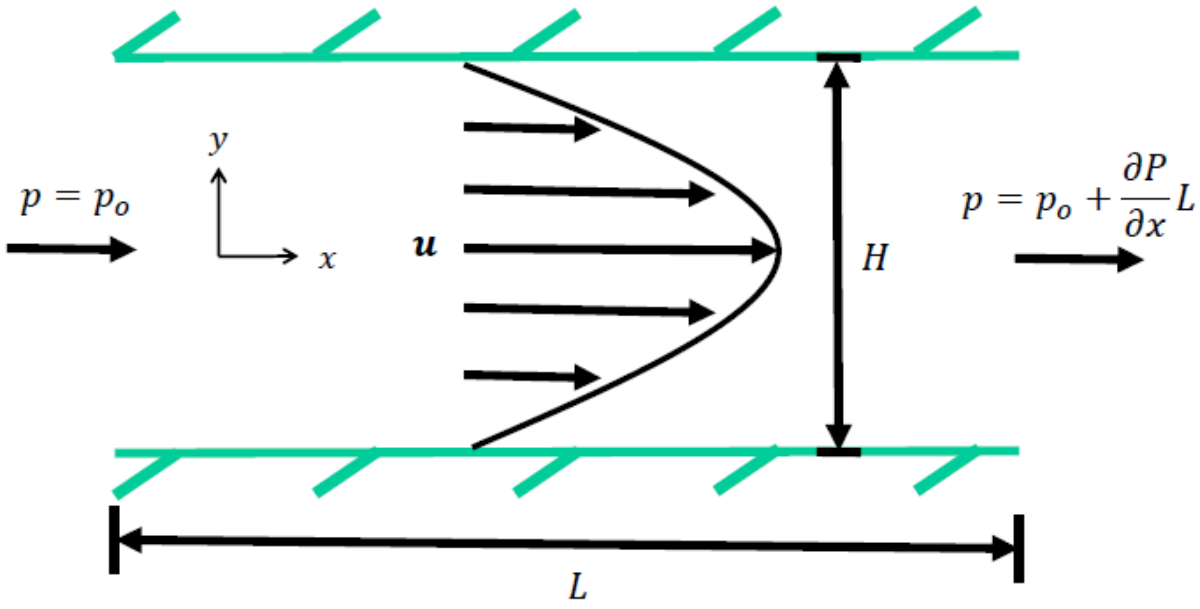

Figure 1.3: Schematic of Poiseuille flow; no-slip boundary conditions are enforced at the top and bottom boundaries, and periodic boundary conditions are enforced at the left and right boundaries. The size of the domain is $L = 32$ and $H = 64$.

in this section were run on a single core of an Intel I7-860 Quad-Core 2.80GHz processor. For the MRT relaxation matrix the free parameters were set to $s_1 = s_2 = s_4 = s_6 = 1.1$, which follows the recommendation of [17] for reasons of stability, and has been successfully used to simulate non-Newtonian flow in the past [7, 37].

1.4.1.1 Bingham Plastic Fluids The Bingham plastic simulations were carried out with a pressure gradient of $\frac{\partial p}{\partial x} = 1.0 \times 10^{-5}$, and a plastic viscosity of $\mu_p = 0.2$. The yield stress was varied between four different values $\tau_y = [4.0, 8.0, 12.0, 16.0] \times 10^{-5}$, and four different LBM schemes were used: (1) BGK with $m = 10^5$, (2) BGK with $m = 10^8$, (3) BGK with $m = 10^8$ and the median filter, and (4) MRT with $m = 10^8$. Recall that m is the stress growth exponent for the Papanastasiou approximation. The relative L_2 and relative L_∞ errors with respect to the analytical solution were computed for each simulation. The analytical solution for Poiseuille flow of a Bingham plastic fluid is given by:

$$u_x(y) = \begin{cases} \frac{1}{2\mu_p}\left(-\frac{\partial p}{\partial x}\right)\left[h^2 - y_\tau^2\right] - \frac{\tau_y}{\mu_p}\left(h - y_\tau\right), & 0 \leq |y| \leq y_\tau, \\ \frac{1}{2\mu_p}\left(-\frac{\partial p}{\partial x}\right)\left[h^2 - y^2\right] - \frac{\tau_y}{\mu_p}\left(h - |y|\right), & y_\tau < |y| \leq h, \end{cases} \tag{1.29}$$

where $y_\tau = -\tau_y / \frac{\partial p}{\partial x}$ is the vertical location at which the fluid yields.

The relative L_2 error, relative L_∞ error, and computation time for each simulation are presented in Table 1.1. The Reynold's number was computed by $Re = \frac{\rho U H}{\mu_p}$, where U is the maximum velocity given by the analytical solution. The Bingham number was computed by $Bn = \frac{\tau_y H}{\mu_p U}$.

As has been reported previously, for the BGK collision operator, using a stress growth exponent of $m = 10^5$ is more accurate with respect to the analytical solution than using a stress growth exponent of $m = 10^8$ [8]. A larger stress growth exponent results in a more accurate Papastasiou approximation of the true Bingham plastic constitutive model, however, it leads to more nonphysical oscillations that degrade the numerical solution for the BGK collision operator. Upon inspection of Table 1.1, it does not appear that entropic

Table 1.1: Bingham plastic Poiseuille flow

Collision Operator	Median Filter	m	τ_y ($\times 10^{-5}$)	Re	Bn	L_2	L_∞	Time (sec)
BGK	No	10^5	4.0	6.05	0.68	0.0062	0.0153	1857
			8.0	4.42	1.85	0.0204	0.0411	2329
			12.0	3.04	4.04	0.0503	0.0891	3345
			16.0	1.92	8.52	0.1161	0.1879	2029
BGK	No	10^8	4.0	6.05	0.68	0.0109	0.0282	2831
			8.0	4.42	1.85	0.0330	0.0670	3509
			12.0	3.04	4.04	0.0788	0.1570	4838
			16.0	1.92	8.52	0.1991	0.3539	3790
BGK	Yes	10^8	4.0	6.05	0.68	0.0100	0.0273	2903
			8.0	4.42	1.85	0.0361	0.0823	3567
			12.0	3.04	4.04	0.2439	0.3832	4800
			16.0	1.92	8.52	0.7533	1.0718	3507
MRT	No	10^8	4.0	6.05	0.68	0.0013	0.0013	5914
			8.0	4.42	1.85	0.0018	0.0018	7908
			12.0	3.04	4.04	0.0026	0.0026	7160
			16.0	1.92	8.52	0.0041	0.0041	5559

median filtering helps mitigate errors that occur as a result of using $m = 10^8$ for Bingham plastic Poiseuille flow. In fact, the median filter resulted in a less accurate solution in all cases other than the case with the lowest yield stress considered (i.e., the smoothest flow field), and rendered the solution altogether useless for the higher yield stress fluids (relative errors of approximately 25-75%).

In general, the BGK collision operator using a stress growth exponent of $m = 10^5$ had the lowest computational time. This can be attributed to the fact that a smoother approximation of the Bingham plastic constitutive model would lead to a solution for μ_{app} converging with less iterations. The BGK collision operator using a stress growth exponent of $m = 10^5$ experienced relatively low error for lower yield stress fluids, however, for $\tau_y = 12 \times 10^{-5}$ and 16×10^{-5} the relative L_∞ errors were 8.9% and 19%, respectively, which is larger than what would be considered acceptable for most engineering applications.

The LBM approximations of the velocity profile across the channel (more specifically, $u_x(\mathbf{x}_j, 25000)$ where $\mathbf{x}_j = \begin{Bmatrix} 16 & y_j \end{Bmatrix}^T$ for $j = 1, 2, ..., 64$, i.e. $\mathbf{x}_j$ is taken at 16 nodes in from the left in the x-direction and for the full height of the channel in the y-direction) for the BGK collision operator using $m = 10^5$ and $m = 10^8$ are plotted with the analytical solution (1.23) in Figure 1.4 and Figure 1.5, respectively. Due to the smoothness of the LBM approximation in Figure 1.4, one can conclude that the error for the BGK model with $m = 10^5$ is not due to nonphysical oscillations, but instead the inaccuracy of the Papastasiou approximation with a lower stress growth exponent. In contrast, the LBM approximation in Figure 1.5 is not smooth, which suggests that the error for the BGK model with $m = 10^8$ is due to nonphysical oscillations.

In order to better understand why median filtering did not eliminate the nonphysical oscillations in high yield stress fluids, but instead exacerbates the problem, it is necessary to investigate what is happening at the particle distribution scale. Figure 1.6 compares particle distributions to quasiequilibrium. More specifically, Figure 1.6 compares $f_i(\mathbf{x}_j, 25000)$ to $f_i^{eq}(\mathbf{x}_j, 25000)$ where $\mathbf{x}_j = \begin{Bmatrix} 16 & y_j \end{Bmatrix}^T$ for $j = 1, 2, ..., 64$, and $i = 5, 8$. It can be seen that in the BGK, $m = 10^8$ solution, that nonphysical oscillations pollute the quasiequilibrium profile as well. These nonphysical oscillations likely originate at the lattice scale due to the sharp gradient in the macroscopic velocity, $\mathbf{u}$, near the walls, and the sharp gradient

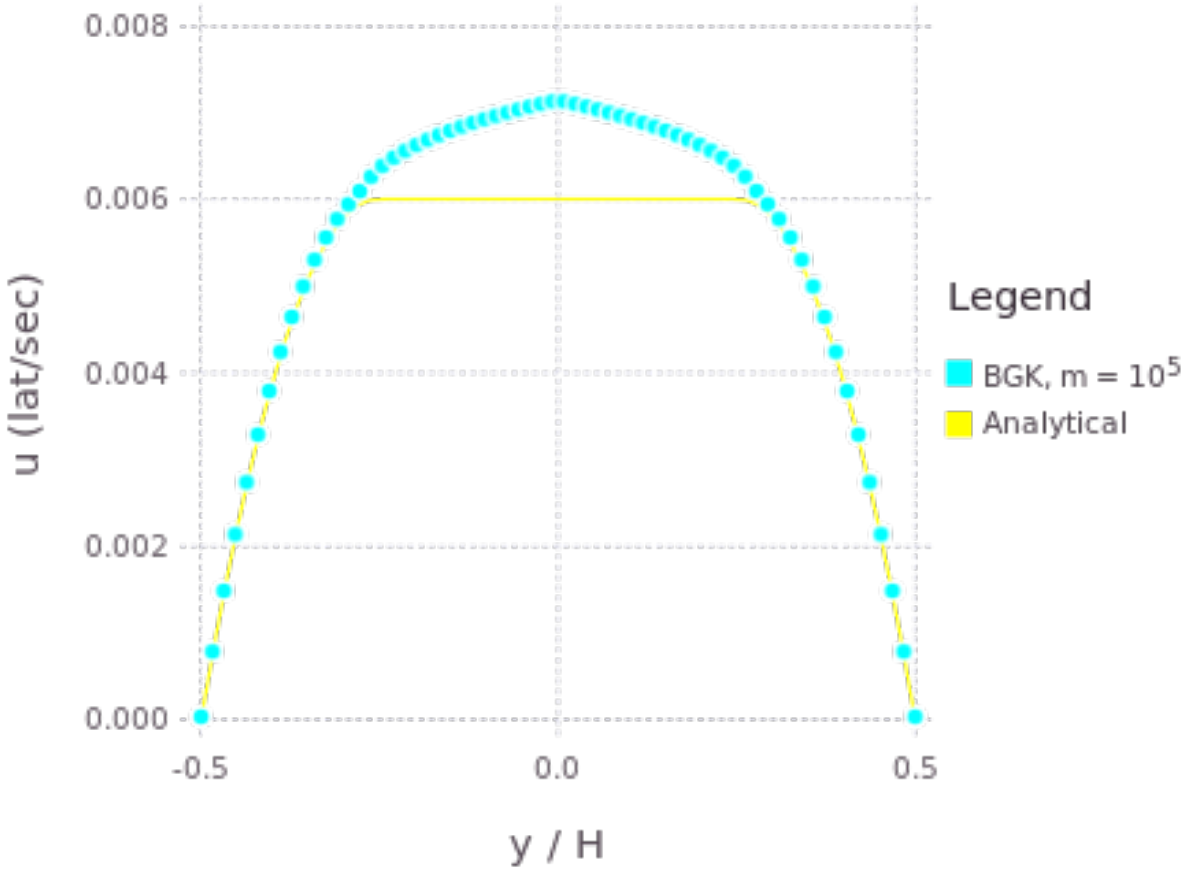

Figure 1.4: LBM approximation using BGK and $m = 10^5$ compared to the analytical solution for $\tau_y = 16 \times 10^{-5}$.

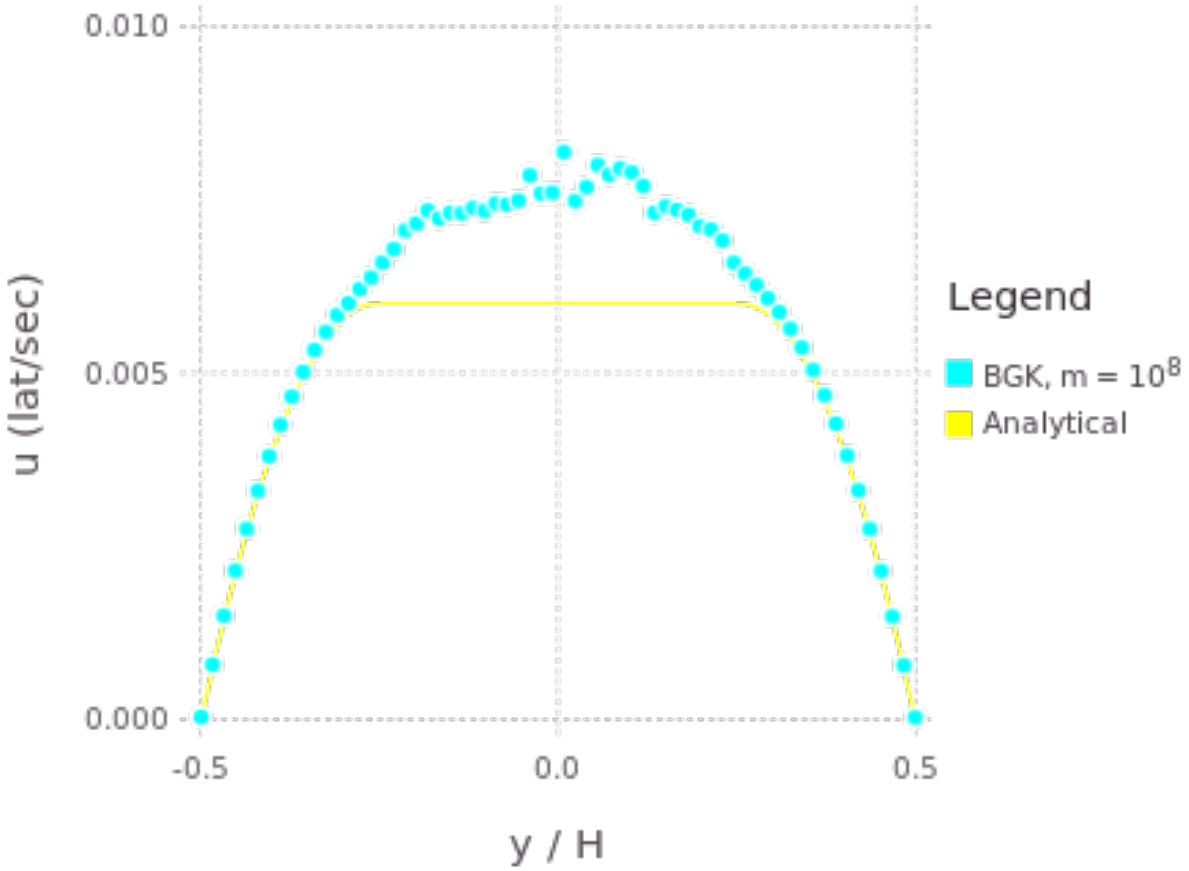

Figure 1.5: LBM approximation using BGK and $m = 10^8$ compared to the analytical solution for $\tau_y = 16 \times 10^{-5}$.

in $\mathbf{u}$ is a result of a sharp gradient in μ_{app}, namely the sharp gradient of the constitutive relationship. Because the nonphysical oscillations make their way into the quasiequilibrium values, entropic median filtering does not help dampen the oscillations but instead contracts the particle distributions closer to the quasiequilibrium oscillations, which explains why the median filtered results were less accurate for Bingham plastic Poiseuille flow. In order to ensure that this phenomena was a side effect of all entropic filtering, and not just entropic median filtering with $\theta = 1.0 \times 10^{-6}$ and $n_s = 2.7$, optimization was used to find the value of θ that minimized error for both median filtering and Ehrenfests' regularization. The optimization problem was defined as follows:

$$\begin{aligned} \min_{\theta} \quad & f(\theta) \\ \text{such that} \quad & \theta \in [10^{-10}, 2.0] \end{aligned}$$

where $f(\theta) \equiv$ the relative L_2 error between the LBM approximation using $m = 10^8$ and entropic filtering with a ΔS threshold of θ (used in the criteria defined in (1.16)). The bounds on θ, namely $\theta \in [10^{-10}, 2]$ represent θ such that 100% of lattice sites are filtered for every time step ($\theta = 10^{-10}$) and θ such that no lattice sites are filtered for any time step ($\theta = 2.0$). The optimization problem was solved for the cases of using median filtering and Ehrenfests' regularization using both Brent's method and the Golden Section search. For all four cases, the optimal solution was $\theta = 2.0$ and the cost function, $f(2.0)$, was equal to the relative L_2 error for the BGK collision operator, $m = 10^8$ and no entropic filtering. The results of the optimization suggest that entropic filtering, at best does not affect the accuracy of LBM, and often adversly affects the accuracy of LBM in approximating Bingham plastic Poiseuille flow, regardless of whether median filtering or Ehrenfests' regularization is used, and regardless of what the ΔS threshold, θ, is set to. Thus, entropic filtering is not effective for increasing the accuracy of Bingham plastic Poiseuille flow.

On average, the LBM model using the MRT collision operator took 2.9 times more computation time than the BGK collision operator with $m = 10^5$. However, the increased computational time can be justified for the MRT collision operator because MRT solution did not suffer from the same level of nonphysical oscillations as the BGK collision operator when using the more accurate approximation of the Bingham plastic model, i.e. when $m = 10^8$.

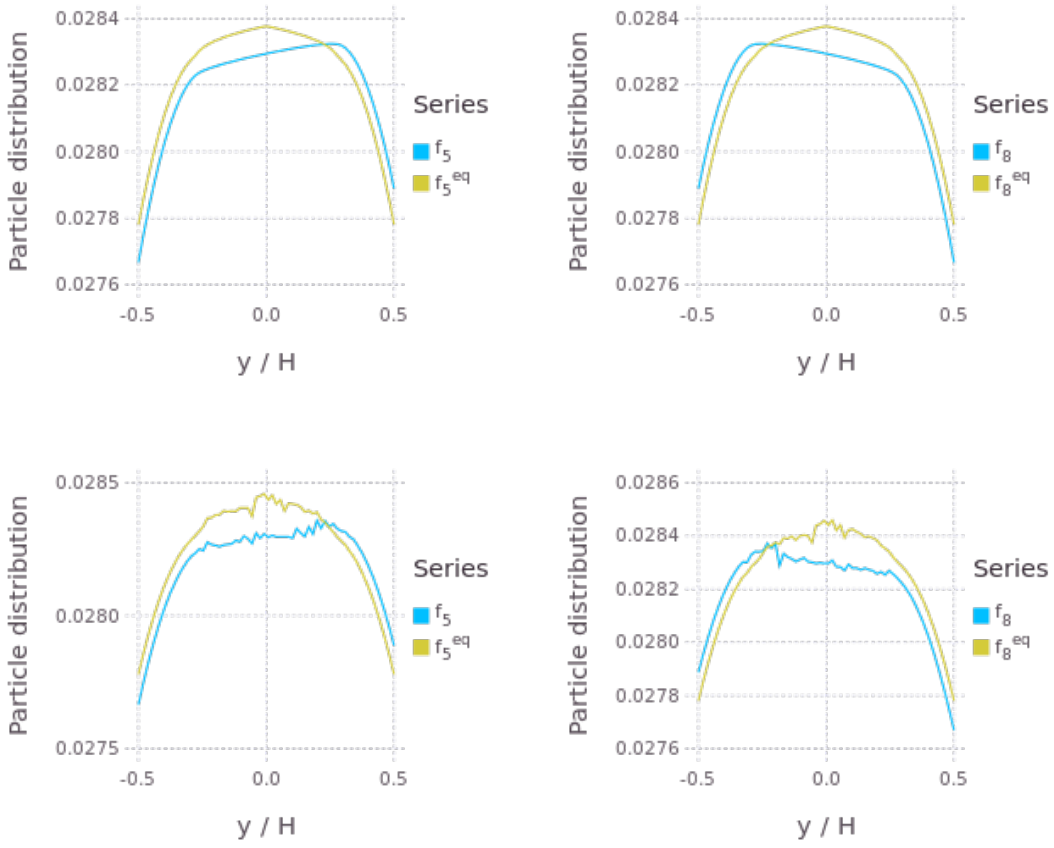

Figure 1.6: Particle distributions in the 5 direction (left) and 8 direction (right) compared to their respective quasiequilibriums. The top two plots are for the BGK with $m = 10^5$, the bottom two are for the BGK with $m = 10^8$.

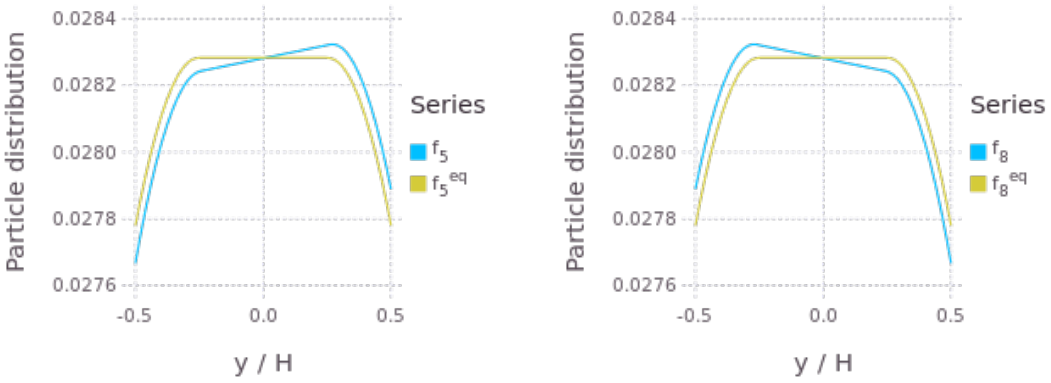

Figure 1.7: Particle distributions in the 5 direction (left) and 8 direction (right) compared to their respective quasiequilibriums for the MRT with $m = 10^8$.

The MRT collision operator was therefore the most accurate solution for all cases. Figure 1.7 compares particle distribution, f_i, profiles to their respective quasiequilbirium profiles, f_i^{eq} for the MRT model; in contrast to the BGK with $m = 10^8$, there are no nonphysical oscillations in the quasiequilibrium distributions.

Another important question to ask is, if the strength of the MRT collision operator is damping out the ghost modes, then are the nonphysical oscillations for the BGK with $m = 10^8$ (with and without median filtering) a result of the ghost modes?. Figure 1.8 shows a measure of the nonequilibrium ϵ moment, $\boldsymbol{\epsilon}^{neq}$, with respect to time for each of the collision schemes, which was calculated as:

$$\frac{||\boldsymbol{\epsilon} - \boldsymbol{\epsilon}^{eq}||_2}{||\boldsymbol{\epsilon}^{eq}||_2} \tag{1.30}$$

where $||\dots||_2$ is the Euclidean norm, $\epsilon_j = 4f_0(\mathbf{x}_j) - 2f_1(\mathbf{x}_j) - 2f_2(\mathbf{x}_j) - 2f_3(\mathbf{x}_j) - 2f_4(\mathbf{x}_j) + f_5(\mathbf{x}_j) + f_6(\mathbf{x}_j) + f_7(\mathbf{x}_j) + f_8(\mathbf{x}_j)$ is related to the square of the energy, and $\mathbf{x}_j = \begin{Bmatrix} 16 & y_j \end{Bmatrix}^T$ for $j = 1, 2, ..., 64$, i.e. $\mathbf{x}_j$ is taken at 16 nodes in from the left in the x-direction and for the full height of the channel in the y-direction. The values measured for the BGK with $m = 10^8$,

with and without median filtering, were significantly higher than for either the MRT or BGK with $m = 10^5$ collision schemes, which suggests that the nonphysical oscillations the BGK with $m = 10^8$ suffered from was in part due to the ϵ moment.

Figure 1.9 shows a measure of the nonequilibrium q_x moment, $\mathbf{q_x}^{neq}$, or energy flux in the x-direction, with respect to time for each of the collision schemes, which was calculated as:

$$\frac{||\mathbf{q_x} - \mathbf{q_x}^{eq}||_2}{||\mathbf{q_x}^{eq}||_2} \tag{1.31}$$

where $q_{x_j} = -2f_1(\mathbf{x}_j) + 2f_3(\mathbf{x}_j) + f_5(\mathbf{x}_j) - f_6(\mathbf{x}_j) - f_7(\mathbf{x}_j) + f_8(\mathbf{x}_j)$ and $\mathbf{x}_j$ were taken across the height of the channel in the same manner as with the ϵ moment. The values measured for the BGK with $m = 10^8$ and median filtered were consistently greater than any other collision scheme. The relative L_2 norm of the $\mathbf{q_x}^{neq}$ for the BGK collision operator with $m = 10^8$ and median filtering solution spent most of the simulation between approximately 50% and 100%, this suggests that the q_x moment was likely the cause of the nonphysical oscillations and error in its solution. As expected (if the dominant source of error in the LBM approximation for Bingham plastic Poiseuille flow is indeed due to the q_x moment), the $\mathbf{q_x^{neq}}$ relative L_2 norm for the BGK with $m = 10^8$ was slightly greater than the BGK with $m = 10^5$, and the $\mathbf{q_x^{neq}}$ relative L_2 was negligible for the MRT collision scheme. These results are consistent with solution error.

It is likely that the nonequilibrium ϵ and q_x moments cause nonphysical oscillations in particle distributions, f_i, with a cumulative effect in time, i.e. osciallations build in amplitude with time. Figure 1.10 and Figure 1.11 show the cumulative measures of the nonequilibrium moments in time, which was calculated as:

$$\int_0^T \frac{||\boldsymbol{\epsilon}(t) - \boldsymbol{\epsilon}^{eq}(t)||_2}{||\boldsymbol{\epsilon}^{eq}(t)||_2} dt, \tag{1.32}$$

and,

$$\int_0^T \frac{||\mathbf{q_x}(t) - \mathbf{q_x}^{eq}(t)||_2}{||\mathbf{q_x}^{eq}(t)||_2} dt, \tag{1.33}$$

where T is the current time. Figure 1.9 and Figure 1.11 shows that both the peak and cumulative values of the relative L_2 norm of $\mathbf{q_x}^{neq}$ are much larger than the peak and cumulative values of the relative L_2 norm of $\boldsymbol{\epsilon}^{neq}$, which suggests that the ghost mode associated with

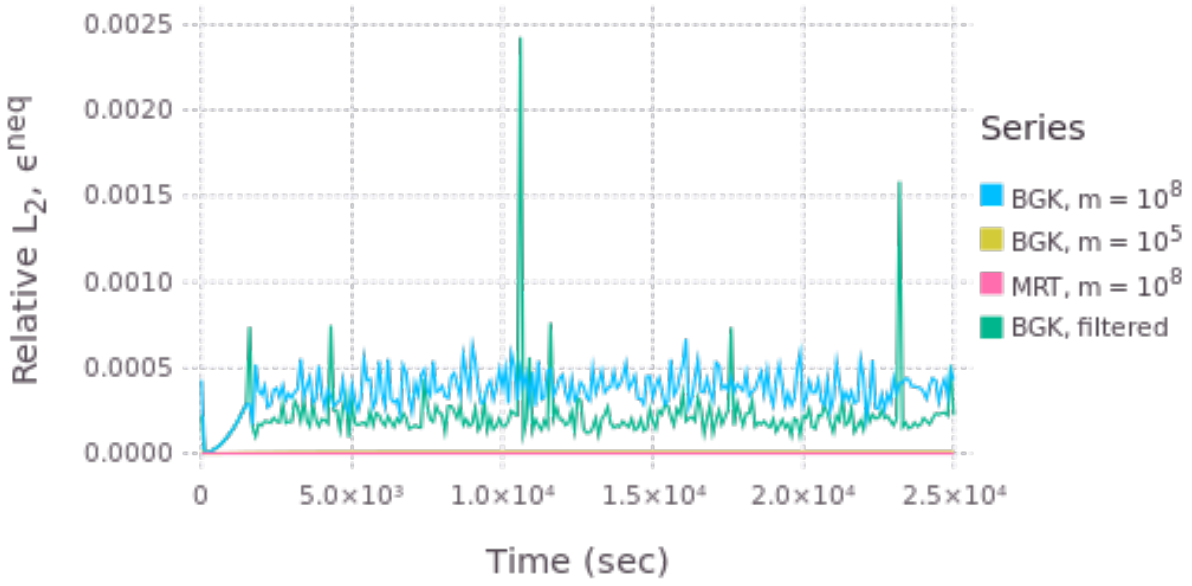

Figure 1.8: Evolution of relative L_2 norm, ϵ^{neq} with time. The norm of the ϵ^{neq} across the height of the channel is an indicator of an increase in oscillations at the lattice level due to the ϵ moment.

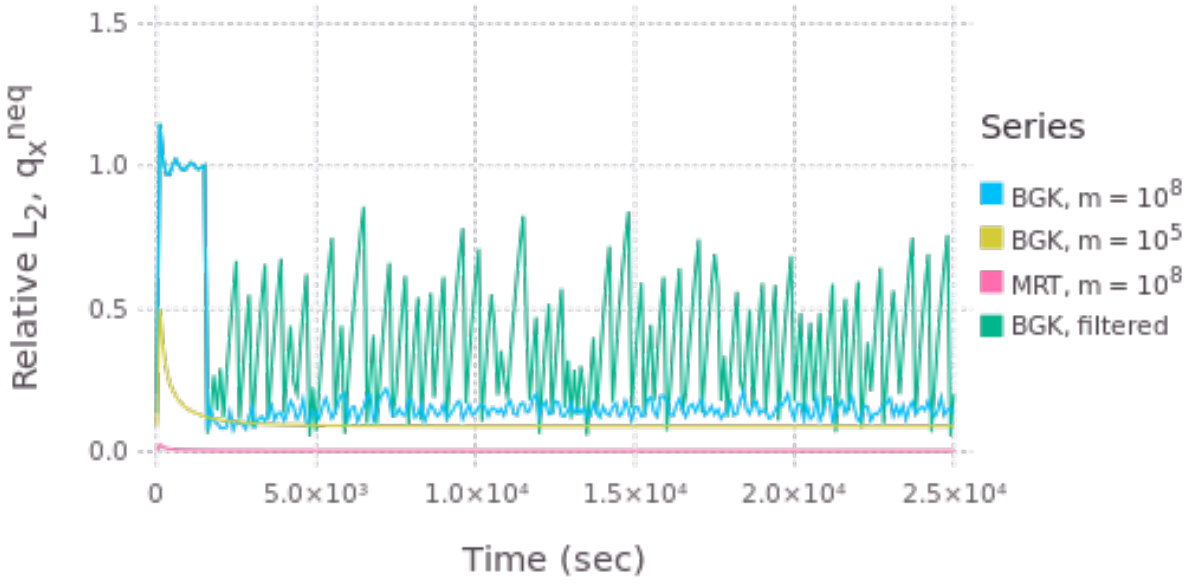

Figure 1.9: Evolution of relative L_2 norm, $\mathbf{q_x}^{neq}$ with time. The norm of the $\mathbf{q_x^{neq}}$ across the height of the channel is an indicator of an increase in oscillations at the lattice level due to the q_x moment.

the q_x moment dominates and is the primary source of oscillations. It can be inferred that the q_x moment was significant source of oscillations in this case because the Poiseuille flow was in the x-direction. If an LBM collision scheme is to be developed for simulating high yield stress, Poiseuille-type flow that is more accurate than the BGK with $m = 10^5$ and more computationally efficient than the MRT, it should focus on a means of dampening the nonequilibrium energy flux moments, namely q_x and q_y.

1.4.1.2 Power-law Fluids The simulations of the Poiseuille flow with the power-law constitutive relationship were carried out with a pressure gradient of $\frac{\partial p}{\partial x} = 1.0 \times 10^{-5}$, and a flow consistency index of $k = 0.2$. The flow behavior index, n, was varied between the four different values: $[0.5, 0.75, 1.25, 1.50]$, and four different LBM schemes were used: (1) BGK, (2) BGK with median filtering, (3) MRT, and (4) BGK-BRT, with ω bounded within $[0.05, 1.995]$. The relative L_2 and relative L_∞ errors with respect to the analytical solution were computed for each simulation. The analytical solution for the velocity profile of Poiseuille flow with the power-law constitutive relationship is given by:

$$u_x(y) = \frac{n}{n+1}\left(-\frac{1}{k}\frac{\partial p}{\partial x}\right)^{1/n}\left[h^{\frac{n+1}{n}} - |y|^{\frac{n+1}{n}}\right]. \tag{1.34}$$

The relative L_2 error, relative L_∞ error, and computation time for each simulation are presented in Table 1.2. The Reynold's number was computed by $Re = \frac{\rho U^{2-n} H^n}{k}$.

Although for $n = 0.5, 0.75, 1.25$ the MRT collision operator was more accurate and required more computation time than the BGK collision operator, for $n = 1.5$ the BGK operator with median filtering required the least computation time and was the most accurate with respect to the analytical solution. In fact, besides for the case of $n = 0.5$, i.e. relatively extreme shear-thinning, the BGK with median filtering was both computationally efficient and accurate. The BGK-BRT had a moderate improvement of accuracy and efficiency–with respect to the regular BGK collision scheme–for flow where the constitutive relationship was only somewhat nonlinear, i.e. for $n = 0.75, 1.25$. Note that none of the collision schemes were sufficiently accurate (error greater than 15%) for the case of $n = 0.5$, and to improve this accuracy it would be necessary to use a different simulation Mach number, a finer grid, and/or a smaller pressure gradient.

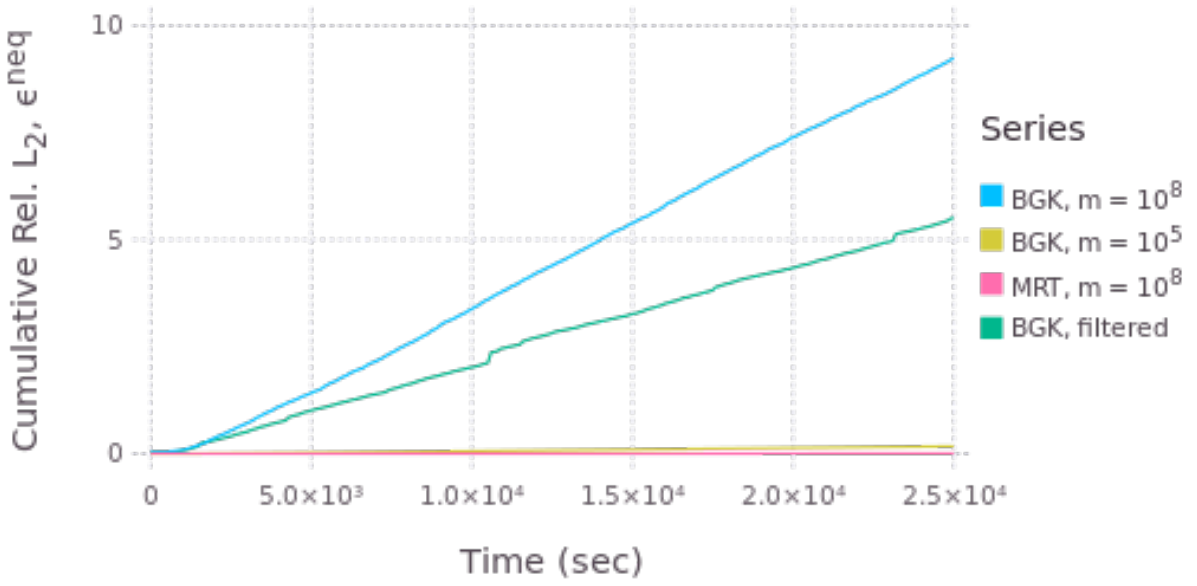

Figure 1.10: Cumulative relative L_2 norm, ϵ^{neq} with time. Oscillations can have a positive effect on each other, building up. The cumulative relative L_2, ϵ^{neq} is a measure of how much oscillations due to the ϵ moment may have been building in time.

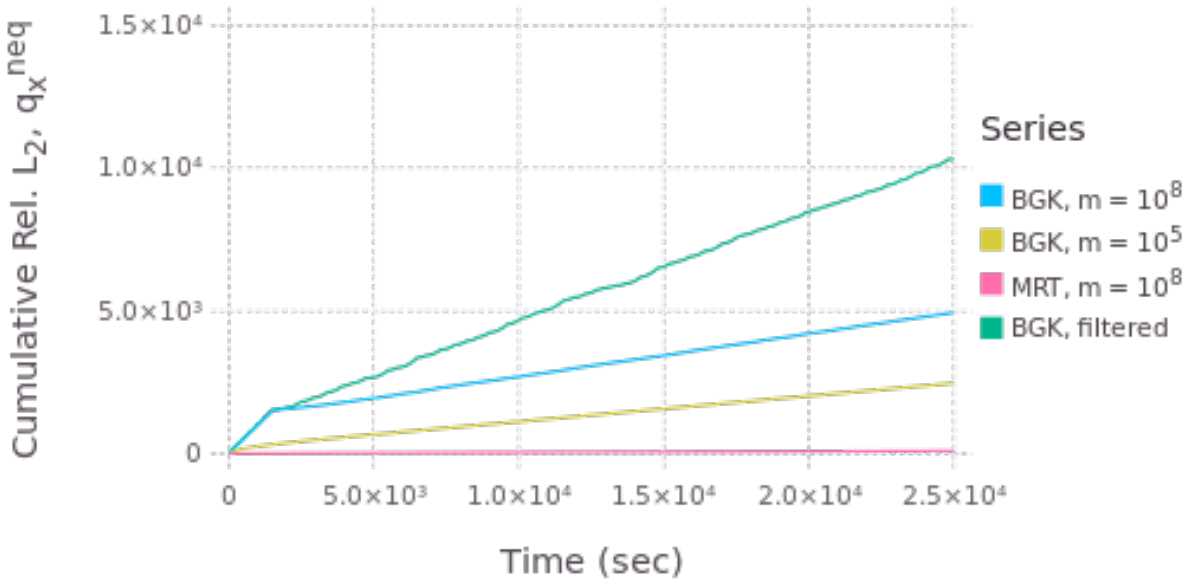

Figure 1.11: Cumulative relative L_2 norm, $\mathbf{q_x^{neq}}$ with time. Oscillations can have a positive effect on each other, building up. The cumulative relative L_2, $\mathbf{q_x^{neq}}$ is a measure of how much oscillations due to the q_x moment may have been building in time.

Table 1.2: Power-law Poiseuille flow

Collision Operator	Median Filter	n	Re	L_2	L_∞	Time (sec)
BGK	No	0.50	0.0007	28.06	30.37	5232
		0.75	0.9125	0.0328	0.0569	2399
		1.25	423.2	0.0051	0.0055	2311
		1.50	2213	1.0	1.0	3622
BGK	Yes	0.50	0.0007	26.72	28.78	5347
		0.75	0.9125	0.0328	0.0569	2385
		1.25	423.2	0.0051	0.0055	2275
		1.50	2213	0.0570	0.0600	2357
MRT	No	0.50	0.0007	0.1758	0.1401	4906
		0.75	0.9125	0.0058	0.0045	4880
		1.25	423.2	0.0051	0.0055	4863
		1.50	2213	1.0	1.0	15992
BGK-BRT	No	0.50	0.0007	11.73	12.56	4450
		0.75	0.9125	0.0320	0.0475	1805
		1.25	423.2	0.0051	0.0055	1905
		1.50	2213	1.0	1.0	8194

1.4.2 Lid-driven Cavity Flow

The lid-driven benchmark was chosen for this numerical study because there are many results available in literature in which to compare with and because the vorticity of the flow coupled with the nonlinear constitutive equations should result in a challenge in terms of stability. Lid-driven cavity flow is generally characterized by a square cavity where a fluid velocity is prescribed tangential to the upper boundary and the remaining boundaries have a no-slip boundary condition. The example of lid-driven cavity flow utilized herein is presented schematically in Figure 1.12.

The lid-driven cavity simulations presented in the section were all simulated on a relatively coarse, 100×100 lattice (other studies simulating lid-driven cavity flow of a non-Newtonian fluid tend to use lattice sizes on the order of 256×256 and 512×512 [8, 42], this study follows that of [27]). A coarse lattice was chosen in order to highlight concerns with stability and accuracy. The simulations were run for either 50000 timesteps or until convergence was met. Convergence was defined by,

$$\sum_{m=1}^{100} \sum_{i,j} \frac{|u_{i,j}^{k} - u_{i,j}^{k-m}|}{|u_{i,j}^{k-m}|} < 1.0 \times 10^{-7}, \tag{1.35}$$

where i is the node index in the x-direction, j is the node index in the y-direction, and k is the current timestep. The lid velocity was prescribed as $u_o = 0.1$. For the MRT relaxation matrix, the free parameters were set to $s_1 = 1.1$, $s_2 = 1.0$, and $s_4 = s_6 = 1.2$ as these values have been successfully applied to simulating lid-driven cavity flow of non-Newtonian fluids in the past [8, 42]. All coordinate values presented in this section (used to describe the location of the center of vortices) are given normalized with respect to the length of the cavity side, i.e. as $(x/L, y/L)$. Note that all results presented as "-" indicate that the tests were numerically unstable to the extent that the degrees of freedom all over the domain were nonsensical.

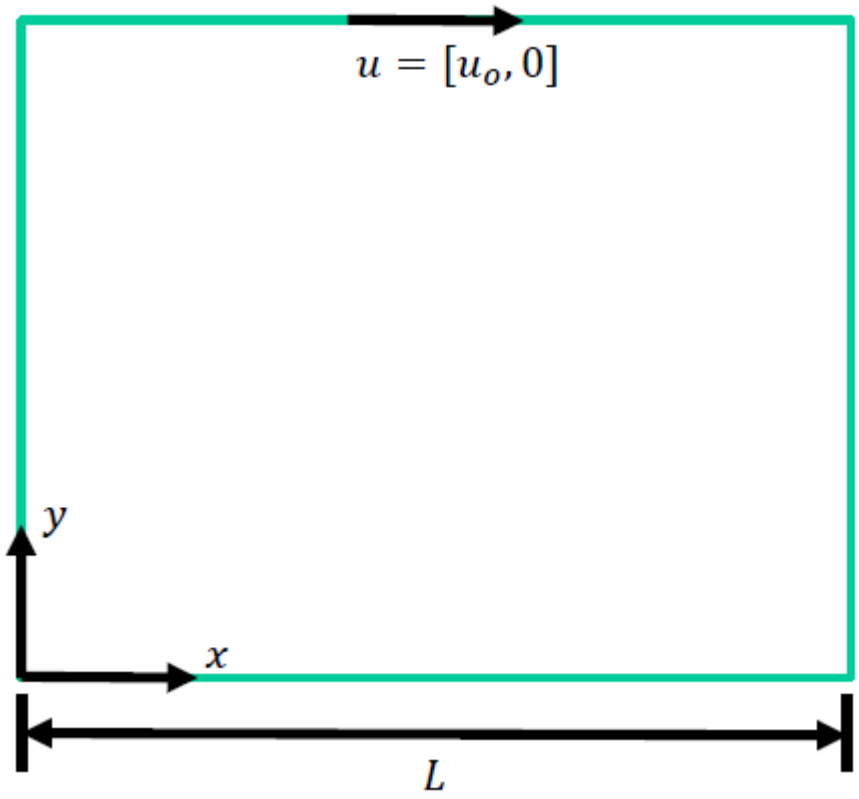

Figure 1.12: Schematic of lid-driven cavity flow; a velocity is prescribed tangential to the top boundary and no-slip is enforced at the remaining boundaries. $L = 100$

1.4.2.1 Bingham Plastic Fluids For the Bingham plastic numerical tests the Reynold's number was varied:$[100, 1000, 5000, 10000]$, and the Bingham number was varied: $[1, 10, 100]$ (Bn and Re were calculated the same as in Section 1.4.1.1). The collision schemes that were tested were: (1) BGK with $m = 10^5$, (2) BGK with $m = 10^8$, (3) BGK-BRT with $m = 10^8$, (4) BGK with $m = 10^8$ and median filtering, (5) MRT with $m = 10^8$ and (6) MRT with $m = 10^8$ and median filtering. Tables 1.3–1.5 compare the center location of the main vortex to literature values taken from [43]. The main vortex location is determined by calculating the stream function using Simpson's rule and finding where it attains a maximum.

Just as before with the Bingham plastic Poiseuille flow, if a modeler is using the BGK collision operator and entropic filtering is not available, a stress growth exponent of $m = 10^5$ yields faster, more accurate results than using a larger stress growth exponent. A smaller stress growth exponent is also more effective at producing accurate results in the BGK collision scheme than placing bounds on the relaxation time (BGK-BRT). However, although the BGK with $m = 10^5$ was the fastest model in all cases, it was also like the other two BGK models without median filtering in that it was unstable for $Re \geq 5000$.

For flow with $Re \geq 5000$, the BGK with $m = 10^8$ and median filtering produced numerically stable results. However, in general, the BGK with $m = 10^8$ and median filtering was consistently different from literature values. The apparent inaccuracy with regards to BGK with $m = 10^8$ and median filtering is probably due to how the numerical stability is enhanced–namely through artificial, nonphysical dissipation. In contrast to the nonphysical nature in which median filtering enhances stability, the stability enhancement used by MRT does not directly affect the macroscopic hydrodynamics of interest, so it again provides a stable, and in most of the cases examined herein, the most accurate solution. The apparent superiority in terms of stability and accuracy of the MRT collision operator still comes at a price though. The MRT collision operator was, in general, 5-10 times slower than any of the BGK collision schemes. The extreme increase in computational expense is probably not due to the collision process itself, i.e. (1.11), but instead calculating the strain-rate (1.22) for each iteration of the solution for μ_{app}.

Table 1.3: Bingham plastic, lid-driven cavity flow; $Bn = 1$.

Bn	Re	Collision Operator	Median Filter	m	Vortex Center (literature)	Vortex Center (LBM)	Time (sec)
1	100	BGK	No	10^5	(0.63, 0.79)	(0.63, 0.79)	17685
		BGK	No	10^8		(0.63, 0.79)	19398
		BGK-BRT	No	10^8		(0.63, 0.79)	22656
		BGK	Yes	10^8		(0.63, 0.79)	21535
		MRT	No	10^8		(0.63, 0.79)	79040
		MRT	Yes	10^8		(0.63, 0.79)	85295
1	1000	BGK	No	10^5	(0.54, 0.57)	(0.54, 0.57)	16109
		BGK	No	10^8		(0.54, 0.57)	17035
		BGK-BRT	No	10^8		(0.54, 0.57)	16879
		BGK	Yes	10^8		(0.54, 0.57)	20170
		MRT	No	10^8		(0.54, 0.57)	46048
		MRT	Yes	10^8		(0.54, 0.57)	55818
1	5000	BGK	No	10^5	(0.52, 0.53)	-	-
		BGK	No	10^8		-	-
		BGK-BRT	No	10^8		-	-
		BGK	Yes	10^8		(0.54, 0.53)	17248
		MRT	No	10^8		(0.51, 0.55)	50572
		MRT	Yes	10^8		(0.52, 0.53)	54225
1	10000	BGK	No	10^5	N/A	-	-
		BGK	No	10^8		-	-
		BGK-BRT	No	10^8		-	-
		BGK	Yes	10^8		(0.56, 0.60)	18186
		MRT	No	10^8		(0.48, 0.48)	43246
		MRT	Yes	10^8		(0.46, 0.54)	50864

Table 1.4: Bingham plastic, lid-driven cavity flow; $Bn = 10$.

Bn	Re	Collision Operator	Median Filter	m	Vortex Center (literature)	Vortex Center (LBM)	Time (sec)
10	100	BGK	No	10^5	(0.53, 0.87)	(0.54, 0.87)	25217
		BGK	No	10^8		(0.55, 0.87)	38285
		BGK-BRT	No	10^8		(0.55, 0.87)	29539
		BGK	Yes	10^8		(0.54, 0.87)	35817
		MRT	No	10^8		(0.53, 0.88)	143741
		MRT	Yes	10^8		(0.54, 0.88)	135059
10	1000	BGK	No	10^5	(0.80, 0.85)	(0.78, 0.83)	11525
		BGK	No	10^8		(0.78, 0.83)	26671
		BGK-BRT	No	10^8		(0.78, 0.83)	19248
		BGK	Yes	10^8		(0.79, 0.84)	34143
		MRT	No	10^8		(0.79, 0.84)	105136
		MRT	Yes	10^8		(0.79, 0.84)	111942
10	5000	BGK	No	10^5	(0.60, 0.55)	-	-
		BGK	No	10^8		-	-
		BGK-BRT	No	10^8		-	-
		BGK	Yes	10^8		(0.52, 0.55)	34638
		MRT	No	10^8		(0.55, 0.55)	111274
		MRT	Yes	10^8		(0.55, 0.53)	121685
10	10000	BGK	No	10^5	N/A	-	-
		BGK	No	10^8		-	-
		BGK-BRT	No	10^8		-	-
		BGK	Yes	10^8		(0.49, 0.54)	19351
		MRT	No	10^8		(0.53, 0.54)	69249
		MRT	Yes	10^8		(0.53, 0.53)	69054

Table 1.5: Bingham plastic, lid-driven cavity flow; $Bn = 100$.

Bn	Re	Collision Operator	Median Filter	m	Vortex Center (literature)	Vortex Center (LBM)	Time (sec)
100	100	BGK	No	10^5	(0.51, 0.95)	(0.51, 0.95)	13237
		BGK	No	10^8		(0.54, 0.96)	26782
		BGK-BRT	No	10^8		(0.53, 0.96)	33095
		BGK	Yes	10^8		(0.58, 0.96)	34430
		MRT	No	10^8		(0.49, 0.95)	161998
		MRT	Yes	10^8		(0.54, 0.96)	162085
100	1000	BGK	No	10^5	(0.53, 0.95)	(0.54, 0.95)	42233
		BGK	No	10^8		(0.64, 0.95)	47364
		BGK-BRT	No	10^8		(0.60, 0.92)	46289
		BGK	Yes	10^8		(0.79, 0.95)	48225
		MRT	No	10^8		(0.54, 0.95)	190119
		MRT	Yes	10^8		(0.55, 0.95)	188242
100	5000	BGK	No	10^5	(0.93, 0.97)	-	-
		BGK	No	10^8		-	-
		BGK-BRT	No	10^8		-	-
		BGK	Yes	10^8		(0.91, 0.95)	57354
		MRT	No	10^8		(0.92, 0.96)	163318
		MRT	Yes	10^8		(0.93, 0.95)	159523
100	10000	BGK	No	10^5	(0.92, 0.94)	-	-
		BGK	No	10^8		-	-
		BGK-BRT	No	10^8		-	-
		BGK	Yes	10^8		(0.84, 0.88)	32080
		MRT	No	10^8		(0.89, 0.91)	152707
		MRT	Yes	10^8		(0.89, 0.91)	145722

In summary for the lid-driven cavity flow of a Bingham plastic fluid,

- for low Reynold's number flow the BGK collision operator with $m = 10^5$ provides an accurate solution with a short computation time,
- for high Reynold's number flow the BGK collision operator requires entropic filtering to remain stable,
- and the MRT collision operator with $m = 10^8$ produces solutions with high accuracy and stability for all of the cases examined herein, but at an increased (approximately 5-10 times more) computational cost.

1.4.2.2 Power-law Fluids For the power-law numerical tests the Reynold's number was varied: $[100, 1000, 5000, 10000]$, and the flow behavior index, n, was varied: $[0.5, 1.5]$ (Re was calculated the same as in Section 1.4.1.2). The collision schemes that were tested were: (1) BGK, (2) BGK-BRT, (3) BGK with median filtering, (4) MRT with $m = 10^8$ and (5) MRT with $m = 10^8$ and median filtering. Table 1.6 and Table 1.7 compare the center location of the main vortex to literature values taken from [42].

For the shear-thinning results, $n = 0.5$, at the lowest Reynold's number considered, $Re = 100$, all of the collision schemes produced results that agreed well with the literature value. However, the solutions became unstable at higher Reynold's numbers and entropic filtering was necessary to produce a stable soltuion when $Re \geq 1000$ for the BGK collision operator, and when $Re \geq 5000$ for the MRT collision operator. Although there still appears to be somewhat of a tradeoff between computational efficiency and accuracy in regards to the BGK with median filtering and MRT with median filtering, it does not seem to be nearly as drastic as when simulating Bingham plastic lid-driven flow; e.g. neither collision scheme consistently agrees with the literature values; and the MRT with median filtering is only 2-3 times slower than the BGK with median filtering. A good example of this tradeoff is the shear-thinning results for $Re = 5000$: the location of the main vortex for the BGK with median filtering differed from literature by more than 10% in both the x and y directions but the MRT with median filtering has approximately twice the computational cost.

Table 1.6: Power-law, lid-driven cavity flow; $n = 0.5$.

n	Re	Collision Operator	Median Filter	Vortex Center (literature)	Vortex Center (LBM)	Time (sec)
0.5	100	BGK	No	(0.72, 0.78)	(0.71, 0.77)	21429
		BGK-BRT	No		(0.71, 0.77)	14547
		BGK	Yes		(0.72, 0.78)	33221
		MRT	No		(0.71, 0.77)	77287
		MRT	Yes		(0.71, 0.77)	110403
0.5	1000	BGK	No	(0.58, 0.55)	-	-
		BGK-BRT	No		-	-
		BGK	Yes		(0.53, 0.59)	24935
		MRT	No		(0.53, 0.54)	72102
		MRT	Yes		(0.53, 0.54)	78300
0.5	5000	BGK	No	(0.53, 0.52)	-	-
		BGK-BRT	No		-	-
		BGK	Yes		(0.63, 0.68)	23517
		MRT	No		-	-
		MRT	Yes		(0.51, 0.58)	54225
0.5	10000	BGK	No	(0.53, 0.52)	-	-
		BGK-BRT	No		-	-
		BGK	Yes		(0.50, 0.55)	22603
		MRT	No		-	-
		MRT	Yes		(0.50, 0.54)	63892

Table 1.7: Power-law, lid-driven cavity flow; $n = 1.5$.

n	Re	Collision Operator	Median Filter	Vortex Center (literature)	Vortex Center (LBM)	Time (sec)
1.5	100	BGK	No	(0.56, 0.73)	(0.57, 0.73)	10897
		BGK-BRT	No		(0.57, 0.73)	6239
		BGK	Yes		(0.56, 0.73)	11847
		MRT	No		(0.56, 0.73)	39017
		MRT	Yes		(0.56, 0.73)	96033
1.5	1000	BGK	No	(0.55, 0.64)	(0.54, 0.61)	19764
		BGK-BRT	No		(0.54, 0.61)	11949
		BGK	Yes		(0.54, 0.61)	24516
		MRT	No		(0.54, 0.61)	58714
		MRT	Yes		(0.54, 0.61)	69884
1.5	5000	BGK	No	(0.53, 0.61)	(0.52, 0.57)	20147
		BGK-BRT	No		(0.52, 0.57)	12116
		BGK	Yes		(0.52, 0.57)	23140
		MRT	No		(0.53, 0.57)	60584
		MRT	Yes		(0.52, 0.58)	58519
1.5	10000	BGK	No	(0.51, 0.55)	(0.53, 0.55)	21570
		BGK-BRT	No		(0.53, 0.55)	12841
		BGK	Yes		(0.53, 0.55)	21570
		MRT	No		(0.49, 0.56)	61453
		MRT	Yes		(0.49, 0.55)	67546

For the shear-thickening results, $n = 1.5$, there were no issues of stability. What is interesting is that all of the collision schemes produce similar results for each of the cases, with the difference in the location of the main vortex being no greater than 1% in either the x or y direction for any two collision schemes (with the exception of the high Reynold's number case, $Re = 10000$). The BGK-BRT consistently needed the least amount of computation time. The reason the BGK-BRT may be the most efficient is that because the collision frequency, ω, is bounded, and consequently μ_{app} is bounded, meaning the solution to the constitutive equation may be converging to a bound with less iterations than the other collision schemes.

1.5 CONCLUSIONS

A numerical investigation into the accuracy, stability, and efficiency of LBM collision models when applied to non-Newtonian flow was presented. The numerical investigation included testing the BGK and MRT collision operators, with and without entropic filtering, as applied to Bingham plastics and power-law fluids. Two different benchmark problems were chosen for the study: Poiseuille flow, and lid-driven square cavity flow. The results showed that:

- For high yield stress fluids in Poiseuille-type flow, only the MRT collision operator did not suffer from nonphysical oscillations.
  - The oscillations appeared to be due to high nonequilibrium values for the moment related to the square of the energy, ϵ, and the energy flux moment in the direction of flow, q_x.
  - If a collision scheme is to be developed for high yield stress, Poiseuille-type flow that is more accurate than the BGK with $m = 10^5$ and more computationally efficient than the MRT, then it should focus on dampening the nonequilibrium energy flux moment.
- Median filtering can be an effective technique for enhancing stability, especially for high Reynold's number flow; however, if the filter is not carefully tuned by properly adjusted

the threshold, δ, or number of standard deviations, n_s, then the physical intregrity, and consquently accuracy, of the model can be adversely impacted.

- In general, the MRT collision operator is much more computationally expensive than its BGK counterpart and is some times even orders of magnitude slower.
- To summarize Bingham plastic, lid-driven cavity flow,
  - for low Reynold's number flow the BGK collision operator with $m = 10^5$ provides an accurate solution with a short computation time,
  - for high Reynold's number flow the BGK collision operator requires entropic filtering to remain stable.
- To summarize power-law, lid-driven cavity flow,
  - for shear-thinning fluids at high Reynold's numbers ($Re \geq 5000$) median filtering is necessary to produce a stable solution,
  - for shear-thickening, lid-driven cavity flow, there is much less concern for numerical instability.

2.0 FREE SURFACE AND NON-NEWTONIAN SIMULATION OF WELLBORE CEMENTING USING THE LATTICE BOLTZMANN METHOD

2.1 ABSTRACT

When oil and gas wellbores are drilled, barriers must be put in place to ensure that fluids do not leak out of the wellbore. An important yet vulnerable barrier is the cement annulus and is created through a process known as primary cementing. Every well has unique subsurface conditions, and so no cement slurry mix design both performs well and is economical for all wells. Computational methods can help better understand primary cementing and aid designers in determining the optimal mix. The lattice Boltzmann method (LBM) is a promising technique for simulating primary cementing because it is well-suited for efficiently simulating non-Newtonian flow, multiphase multicomponent flow, and flow through complex geometries–namely, some of the complexities associated with the mechanics of primary cementing. In Section 2.3, an algorithm for simulating non-Newtonian free-surface flow using LBM is presented. The algorithm was implemented and used to study primary cementing of a dry annulus, i.e. an annulus that is not filled with drilling mud. More specifically, the study involved parameterizing different cement slurry flows and investigating how well each slurry flow filled different wellbore geometries. The study is followed by conclusions and a discussion of future work.

2.2 INTRODUCTION

Of critical importance to drilling operations of all kinds is that barriers are placed to prevent gasses and fluids from migrating from one geological zone to another (i.e., zonal isolation is achieved) [44–48]. If zonal isolation is not achieved, gasses and fluids may migrate through the well to the surface and up into the atmosphere–potentially causing pollution, or at the very least, contributing to an increase in greenhouse gasses–or, worse yet, formation gasses and fluids can migrate into aquifers, potentially harming wild life and people. Furthermore, it can be argued that the most important, yet vulnerable, barrier in terms of achieving zonal isolation of a wellbore is the cement annulus that is created between the casing and the formation. There are various mechanisms by which this cement annulus can fail. According to previous studies [48–54], the most prevalent failure mechanisms of the cement annulus are:

- Stresses developing in the cement annulus as a result of temperature gradients, moisture gradients, overburden pressure, and chemical shrinkage of the cement matrix. These stresses can cause cracking in the cement, or debonding at either the casing–cement or cement–formation interfaces.
- Poor fill of the annulus. If cement slurry does not fill the annulus and if drilling mud is left behind the mud can dry, crack, and provide a weak path for fluids and gasses under pressure to push through, or if a dry hole is cemented and not filled properly, fluids and gasses can travel through channels and voids left in the annular space.
- Gas channeling through the annulus during cement curing. Initially, after the annulus is poured, the cement column transmits its full hydrostatic pressure against the rock formation. As the cement annulus hydrates, it solidifies, becoming stiffer and more self-supporting. When the column begins to support itself, the hydrostatic pressure of the cement column–against the rock formation–begins to drop. If the hydrostatic pressure of the cement column drops below the pressure of a formation gas before the cement annulus has developed adequate strength to resist it, the formation gas can penetrate into the cement annulus and form channels, or degrade the cement annulus in other ways.

In order to better understand, and thus improve primary cementing for zonal isolation, several works have attempted to model certain aspects of the multiphase and multiphysics processes of wellbore cement placement. For example, [55] developed a mathematical model to describe the displacement of drilling mud by the the cement slurry during primary cementing. Among their assumptions were that the flow as laminar, the process could be modeled in a quasi-steady manner, the volumetric flow rate was constant at each cross section of the flow, and the pressure fields were only dependent on the distance from the center of the annulus to either the rock formation or steel casing surface. The model was then used to explore the effect of various parameters on the displacement efficiency of the spacer, such as the density ratio between the mud and the spacer, the viscosity ratio between the mud and the spacer, the displacement rate, the displaced phase yield stress, and the displacing phase yield stress. It was concluded that displacement efficiency could be improved by increasing the density of the displacing phase, increasing the viscosity of the displacing phase, (in general) decreasing the displacement rate, decreasing the yield stress of the displaced phase, and increasing the yield stress of the displacing phase. [49] developed a mathematical model for primary cementing of an oil well using a Hele-Shaw displacement model. The model was more general than the model developed by [55] as it used less restrictive assumptions and was able to consider an eccentric annulus. The bulk fluid motion of the spacer and drilling mud during primary cementing were investigated. The intended use of the model was not to make general statements about what properties of the spacer and drilling mud were desirable, but to instead be used iteratively during the design process for the cement job. Results showed that the model was able to simulate an unyielded channel of mud left on the narrow side of the annulus. [54] used a computational fluids dynamics (CFD) solver with volume of fluid (VOF) method to simulate the cementing process of a 50 ft. section of wellbore. The model included the interfacial dynamics of, not just the spacer and drilling mud, but also the cement slurry–which was not considered in either [55] or [49]. The drilling mud and cement slurry properties were kept constant, while the spacer density, viscosity, and displacement rates were varied. [54] concluded that the high displacement efficiency occurred when the spacer was the same density as the drilling mud and had a smaller viscosity, similar to that of water. The displacement efficiency was poor for all scenarios in which the spacer and

cement slurry densities were equal. [20] developed a model simulating primary cementing using the Lattice Boltzmann Method. [20] used the model to investigate the shape of the interface between the displacing phase (i.e. cement slurry) and displaced phase (i.e. drilling mud) in a horizontal, eccentric annulus. It was found, in general, that a greater density ratio between the displacing phase and displaced phase and lower eccentricity results in better displacement in a horizontal, eccentric annulus.

Overall, past studies have tended to idealize the rock formation as a straight wall. Although this is a desirable simplification to make for capturing bulk fluid phenomena, it does not accurately describe what is happening locally at the surface of the rock formation. Flow near the surface of the formation, and in and around the imperfections of the formation geometry, could influence the bond of the cement annulus to the rock formation, and the fill of the cement slurry very near to the rock formation. If an adequate bond does not develop, debonding can occur as a result of thermal and mechanical stresses. Even if most of the annulus is filled by the cement slurry, a small gap at the cement–formation interface that stretches for a long enough span of the wellbore would still be susceptible to fluid and gas migration, i.e. loss of zonal isolation. One could even argue that the characteristic of the cement slurry flow is most important local to the cement–formation interface, and that considering imperfections in the rock formation is imperative to determining whether zonal isolation has been achieved.

The purpose of the current work is to develop a computational approach to investigate the flow of cement slurry in and around the–possibly–imperfect features of a rock formation in a vertical section of a wellbore, with the hope of better understanding what parameters of the primary cement job will lead to a good fill of the cement annulus and high bond strength at imperfect rock formation features. The Lattice Boltzmann Method (LBM) was chosen

as the most suitable modeling technique for the desired purpose because of its ability to model flow through and around complex geometries [56], such as those found at the surface of the rock formation. LBM also has other advantages as an approach for simulating primary cementing:

- LBM is well-suited for simulating non-Newtonian fluids because the strain-rate tensor is computed local to each node and is second-order accurate [4, 39]. Many fluids present in primary cementing such as the spacer, drilling mud, and most importantly, the cement slurry, are best modeled as non-Newtonian fluids.
- LBM is well-suited for simulating multiphase multicomponent flow and free-surface flow because it can handle complicated interface shapes between fluid phases and components.
- LBM is easily written in parallel. As hardware architectures shift from one or a few cores to several CPUs, it becomes increasingly important that code for simulating complex and computationally expensive phenomena be written in parallel.

The current work focuses on the problem of cementing a dry hole, i.e. an annulus that is not filled with drilling mud prior to cementing. In order to numerically investigate this problem, an LBM model for non-Newtonian and free-surface flow is developed. The details of the LBM model are outlined in Section 2.3. What follows in Section 2.4 is a preliminary study on how different characteristics of flow, e.g. cement slurry yield stress, cement slurry inlet velocity, etc., perform in regards to fill of the annulus for different wellbores with imperfect rock formation geometries. Section 2.5 outlines conclusions resulting from the numerical study and a discussion of future work.

2.3 NUMERICAL METHODS

2.3.1 Lattice Boltzmann Method

For the sake of computational efficiency, the numerical study considered a two-dimensional section of the wellbore and was simulated using the D2Q9 lattice. Idealizing the annulus as two-dimensional limits the modeling approach in that annulus eccentricity and other

three-dimensional phenomena could not be considered. A two-dimensional representation of the annulus was deemed sufficient as the focus of this study is to establish the Lattice Boltzmann Method as a suitable method for simulating primary cementing in an annulus with an imperfect rock formation surface. In addition to using a D2Q9 lattice, the BGK collision operator used was in the current chapter. For more details on the fundamentals of the Lattice Boltzmann Method, the D2Q9 lattice, or the BGK collision operator, see Section 1.3.

2.3.2 Cement Slurry Constitutive Relationship

Cement slurry is typically modeled using a non-Newtonian constitutive relationship. As is commonly utilized for modeling cement and concrete fluid dynamics [19, 57–61], the Bingham plastic constitutive relationship was utilized herein. Bingham plastics are characterized by a plastic viscosity, which is analogous to the dynamic viscosity for Newtonian fluids, and a yield stress, which is a stress threshold that, if the shear stress does not exceed, the strain-rate is zero. The Bingham plastic constitutive model is difficult to work with numerically. Therefore, a smooth approximation, specifically the Papastasiou approximation, is often used [5, 8, 10, 41, 62, 63] and is used herein. Throughout this chapter, the Papastasiou approximation with a stress growth exponent of $m = 10^6$ is used. The BGK collision operator with $m = 10^6$ can be seen as a compromise between computational efficiency and accuracy for simulating Bingham plastic flow. For more detail on Bingham plastics or the Papastasiou approximation, see Section 1.3.7.1.

2.3.3 Free Surface Flow

A free-surface flow is a flow in which two-fluids exist but the dynamics of one fluid does not need to be explicitly modeled. Typically, the phase of the primary fluid, or the fluid of interest, is a liquid; and the secondary phase that does not need to be explicitly modeled is a gas, often times air at atmospheric pressure. The primary fluid is modeled using a standard CFD method, such as LBM, and the interaction of the secondary fluid on the primary fluid is modeled as a boundary condition at the interface between the two fluids. The

interface is what is referred to as the free-surface. The advantage of modeling a multiphase multicomponent flow as a free-surface is that, because the dynamics of the secondary fluid are not explicitly tracked and simulated, the resulting algorithm is more computationally efficient in terms of both memory and CPU overhead. The algorithm for extending the Lattice Boltzmann Method for free-surface flow used in this work follows the algorithm developed and presented in [64] and [65].

2.3.4 Capturing the Free-Surface

Consider at each node a cell of size $\mathrm{d}x \times \mathrm{d}x$ where $\mathrm{d}x$ is the distance between nodes and the cell is centered at the node. In order to track where the primary fluid is and where it is not (i.e. which cells contain the primary fluid), a variable is introduced, ϵ, which describes what fraction of the cell is covered by the primary fluid. Cells that have a fluid fraction of $\epsilon = 0$ contain no primary fluid (i.e. are empty); cells that have a fluid fraction of $\epsilon = 1$ are filled; and cells that have a fluid fraction $0 < \epsilon < 1$ are neither completely filled nor are they completely empty. The fluid fraction concept is similar to how fluids are tracked in Volume of Fluid (VOF) methods.

2.3.4.1 Mass Transfer It is important to note that the particle distributions, $f_0, ..., f_8$, cannot be used to directly determine the fluid fraction of a cell. Neither can the zeroth velocity moment of the particle distributions, $\rho = \sum_i f_i$. For the algorithm used in this work, $\epsilon(\mathbf{x}, t) \neq \epsilon(\mathbf{f}(\mathbf{x}, \mathbf{t}), \rho(\mathbf{x}, t))$. Instead, each f_i is related to the amount of primary fluid advection in each of the $\boldsymbol{\xi}_i$ discrete velocity directions. To track the fluid fraction and how it changes, another variable is introduced, $M(\mathbf{x}, t)$, which denotes the (primary) fluid mass in each cell. The fluid mass is related to the fluid fraction by $\epsilon = M/\rho$. The change in mass, $\Delta M(\mathbf{x}, t)$ is related to $\mathbf{f}(\mathbf{x}, t)$ and particle distribution in the neighborhood of $\mathbf{x}$. Given initial conditions on $M(\mathbf{x}, 0)$ and a fixed time step size Δt, the fluid mass is determined by $M(\mathbf{x}, t_n) = M(\mathbf{x}, 0) + \Delta t \sum_{k=1}^{n} \Delta M(\mathbf{x}, t_k)$. What remains to track the fluid mass is to develop an expression for $\Delta M(\mathbf{x}, t)$.

2.3.4.2 Cell States Each of the cells in the domain are assigned one of three states: fluid, interface, or gas. The set of fluid, interface, and gas cells are denoted by $\mathcal{F}$, $\mathcal{I}$, and $\mathcal{G}$, respectively. A fluid cell is a cell that is entirely covered by the primary fluid; and a gas cell is a cell that is completely empty, or does not contain any primary fluid. An interface is partially covered, and there is always a layer of interface cells between fluid and gas cells so that a fluid cell and a gas cell are never neighbors. The change in mass is calculated for fluid and interface cells (i.e. $\mathbf{x} \in \mathcal{F} \cup \mathcal{I}$) for each discrete velocity direction as follows:

$$\Delta M_i(\mathbf{x},t) = \begin{cases} f_{\bar{ß}}(\mathbf{x}+\boldsymbol{\xi}_i\Delta t,t) - f_i(\mathbf{x},t), & \mathbf{x} \in \mathcal{F} \text{ or } \mathbf{x}+\boldsymbol{\xi}_i\Delta t \in \mathcal{F} \\ \frac{\epsilon(\mathbf{x},t)+\epsilon(\mathbf{x}+\boldsymbol{\xi}_i\Delta t,t}{2}(f_{\bar{ß}}(\mathbf{x}+\boldsymbol{\xi}_i\Delta t,t) - f_i(\mathbf{x},t)), & \mathbf{x} \in \mathcal{I} \text{ and } \mathbf{x}+\boldsymbol{\xi}_i\Delta t \in \mathcal{I} \\ 0, & \mathbf{x}+\boldsymbol{\xi}_i\Delta t \in \mathcal{G} \end{cases} \quad (2.1)$$

where $\boldsymbol{\xi}_{\bar{ß}}$ represents the discrete velocity vector that is opposite in direction to $\boldsymbol{\xi}_i$ (i.e. $\boldsymbol{\xi}_{\bar{ß}} = -\boldsymbol{\xi}_i$). (2.1) states that when the border of the two cells is covered with fluid, the change in mass for a discrete velocity direction is equal to the difference of the particle distribution entering the cell from the opposite direction and particle distribution leaving the cell in that direction. When the border of the two cells are not covered with fluid (i.e. when both cells are interface cells) the difference is weighted by the average fluid fraction of the two cells because mass is only able to transfer across the fraction of the cell border that is covered in fluid. The total change in mass for a cell is simply $\Delta M(\mathbf{x},t) = \sum_i \Delta M_i(\mathbf{x},t)$. Finally, note that $\Delta M_i(\mathbf{x},t) = -\Delta M_{\bar{ß}}(\mathbf{x}+\boldsymbol{\xi}_i\Delta t,t)$ for all $\mathbf{x} \in \mathcal{X}$ where $\mathcal{X}$ is the domain. As a consequence, it is clear that $\sum_{\mathbf{x}\in\mathcal{X}} \Delta M(\mathbf{x},t) = 0$ (i.e. that mass is conserved for the mass transfer step).

Tracking the transport of mass throughout the domain is an important step in determining what parts of the domain contain the primary fluid and what do not. However, for the free-surface to change shape and propagate, cells need to be able to transition state. Cell states change based on the rule set presented in Table 2.1 where δ_{trans} is a small, computational constant that keeps cells from transitioning back and forth between fluid and interface, or interface and gas states in subsequent time steps. To summarize Table 2.1, gas cells cannot transition to fluid cells and vice versa, interface cells transition to fluid cells when their mass has exceeded ρ by a computational constant, and gas cells when their mass is less than

Table 2.1: Cell state transition rules.

Current State	**Condition**	**Transition**
$(\mathbf{x}, t) \in \mathcal{I}$	$M(\mathbf{x}, t) < -\delta_{trans}$	$(\mathbf{x}, t + \Delta t) \rightarrow \mathcal{G}$, $M(\mathbf{x}, t + \Delta t) = 0$
	$M(\mathbf{x}, t) > \delta_{trans} + \rho(\mathbf{x}, t)$	$(\mathbf{x}, t + \Delta t) \rightarrow \mathcal{F}$, $M(\mathbf{x}, t + \Delta t) = \rho(\mathbf{x}, t + \Delta t)$
$(\mathbf{x}, t) \in \mathcal{F}$	$(\mathbf{x} + \boldsymbol{\xi}_i \Delta t, t + \Delta t) \in \mathcal{G}$ for any $i = 1, 2, ..., 8$	$(\mathbf{x}, t + \Delta t) \rightarrow \mathcal{I}$
$(\mathbf{x}, t) \in \mathcal{G}$	$(\mathbf{x} + \boldsymbol{\xi}_i \Delta t, t + \Delta t) \in \mathcal{F}$ for any $i = 1, 2, ..., 8$	$(\mathbf{x}, t + \Delta t) \rightarrow \mathcal{I}$

zero minus a computational constant. In addition, fluid cells and gas cells transition to the interface state in order to maintain continuity of the interface, i.e. to ensure there is always a layer of interface cells in between fluid cells and gas cells. An example of a cell transitioning state is depicted in Figure 2.1.

2.3.4.3 Updating Cell States and Mass Redistribution The rules for updating cell states in Table 2.1 are fairly intuitive, however, there are some details that must be considered in order to ensure mass is properly conserved and interface continuity is achieved (e.g. note that if the rules outlined in Table 2.1 are followed naively that mass is not conserved when interface cells transition to fluid cells or gas cells). The algorithm for updating cell states follows that which was presented in [65]. It is presented here as Algorithm 1 for the sake of completeness and for outlining minor modifications.

Algorithm 1 Update Cell States and Mass Redistribution

procedure UPDATESTATES

Initialize (empty) data structure, $\mathcal{I}_f$ ▷ $\mathcal{I}$ cells to be transitioned to $\mathcal{F}$
Initialize (empty) data structure, $\mathcal{I}_g$ ▷ $\mathcal{I}$ cells to be transitioned to $\mathcal{G}$
Initialize variable that represents global excess mass, $M_{gex} = 0$

for all cells $\mathbf{x} \in \mathcal{I}$ **do** ▷ Mark interface cells to transition
  if $M(\mathbf{x}, t) < -\delta_{trans}$ **then**
    Add $\mathbf{x}$ to $\mathcal{I}_f$
  else if $M(\mathbf{x}, t) > \rho(\mathbf{x}, t) + \delta_{trans}$ **then**
    Add $\mathbf{x}$ to $\mathcal{I}_g$
  end if
end for

for all cells $\mathbf{x} \in \mathcal{I}_f$ **do**
    ▷ Prepare neighborhoods of $\mathcal{I}$ cells that are to be transitioned to $\mathcal{F}$ cells
  Calculate the average density, ρ_{avg}, of the neighborhood
  Calculate the average velocity, $\mathbf{u}_{avg}$, of the neighborhood
  for all cells $\mathbf{x}_n$ in the neighborhood of $\mathbf{x}$ **do**
    if $\mathbf{x}_n \in \mathcal{G}$ **then**
      Transition $\mathbf{x}_n$ from a $\mathcal{G}$ state to $\mathcal{I}$ state
      $f_i(\mathbf{x}_n, t) = f_i^{eq}(\rho_{avg}, \mathbf{u}_{avg})$
    else if $\mathbf{x}_n \in \mathcal{I}_g$ **then**
      Remove $\mathbf{x}_n$ from $\mathcal{I}_g$ ▷ Ensure interface is continuous
    end if
  end for
end for

for all cells $\mathbf{x} \in \mathcal{I}_g$ **do**
    ▷ Prepare neighborhoods of $\mathcal{I}$ cells that are to be transitioned to $\mathcal{G}$ cells
  for all cells $\mathbf{x}_n$ in the neighborhood of $\mathbf{x}$ **do**
    if $\mathbf{x}_n \in \mathcal{F}$ **then**
      Transition $\mathbf{x}_n$ from a $\mathcal{F}$ state to $\mathcal{I}$ state
    end if
  end for
end for

31: **for all** cells $\mathbf{x} \in \mathcal{I}_f$ **do**

▷ Transition from $\mathcal{I}$ to $\mathcal{F}$ and redistribute excess mass

32: Let $M_{ex} = M(\mathbf{x}, t) - \rho(\mathbf{x}, t)$

33: Approximate the unit normal from the interface toward empty space,

$$\mathbf{n} = \frac{1}{2} \begin{Bmatrix} \epsilon_{i-1,j} - \epsilon_{i+1,j} \\ \epsilon_{i,j-1} - \epsilon_{i,j+1} \end{Bmatrix}$$

▷ Central difference of fluid fraction

34: Initialize $v_{sum} = 0$

35: Initialize (empty) data structure, $\mathcal{I}_r$

36: **for all** cells $\mathbf{x}_n$ in the neighborhood of $\mathbf{x}$ **do**

37: **if** $\mathbf{x}_n \in \mathcal{I}$ **then**

38: Add $\mathbf{x}_n$ to $\mathcal{I}_r$

39: Let $v_i = \begin{cases} \mathbf{n} \cdot \boldsymbol{\xi}_i, & \mathbf{n} \cdot \boldsymbol{\xi}_i > 0 \\ 0, & \text{otherwise} \end{cases}$

40: $v_{sum} = v_{sum} + v_i$

41: **end if**

42: **end for**

43: **if** $v_{sum} > 0$ **then**

44: **for all** cells $\mathbf{x}_j \in \mathcal{I}_r$ **do**

45: $M(\mathbf{x}_j, t) = M(\mathbf{x}_j, t) + M_{ex} \frac{v_i}{v_{sum}}$

46: **end for**

47: **else if** $v_{sum} = 0$ and $\mathcal{I}_r \neq \emptyset$ **then**

48: Let n_r be the number of cells in $\mathcal{I}_r$

49: **for all** cells $\mathbf{x}_j \in \mathcal{I}_r$ **do**

50: $M(\mathbf{x}_j, t) = M(\mathbf{x}_j, t) + \frac{M_{ex}}{n_r}$

51: **end for**

52: **else**

53: $M_{gex} = M_{gex} + M_{ex}$

54: **end if**

55: Transition $\mathbf{x}$ from an $\mathcal{I}$ state to $\mathcal{F}$ state

56: Set $M(\mathbf{x}, t) = \rho(\mathbf{x}, t)$

57: **end for**

for all cells $\mathbf{x} \in \mathcal{I}_g$ **do**

▷ Transition from $\mathcal{I}$ to $\mathcal{G}$ and redistribute excess mass

Let $M_{ex} = M(\mathbf{x}, t)$

Approximate the unit normal from the interface toward empty space,

$$\mathbf{n} = \frac{1}{2} \begin{Bmatrix} \epsilon_{i-1,j} - \epsilon_{i+1,j} \\ \epsilon_{i,j-1} - \epsilon_{i,j+1} \end{Bmatrix}$$ ▷ Central difference of fluid fraction

Initialize $v_{sum} = 0$

Initialize (empty) data structure, $\mathcal{I}_r$

for all cells $\mathbf{x}_n$ in the neighborhood of $\mathbf{x}$ **do**

if $\mathbf{x}_n \in \mathcal{I}$ **then**

Add $\mathbf{x}_n$ to $\mathcal{I}_r$

Let $v_i = \begin{cases} -\mathbf{n} \cdot \boldsymbol{\xi}_i, & \mathbf{n} \cdot \boldsymbol{\xi}_i < 0 \\ 0, & \text{otherwise} \end{cases}$

$v_{sum} = v_{sum} + v_i$

end if

end for

if $v_{sum} > 0$ **then**

for all cells $\mathbf{x}_j \in \mathcal{I}_r$ **do**

$M(\mathbf{x}_j, t) = M(\mathbf{x}_j, t) + M_{ex} \frac{v_i}{v_{sum}}$

end for

else if $v_{sum} = 0$ and $\mathcal{I}_r \neq \emptyset$ **then**

Let n_r be the number of cells in $\mathcal{I}_r$

for all cells $\mathbf{x}_j \in \mathcal{I}_r$ **do**

$M(\mathbf{x}_j, t) = M(\mathbf{x}_j, t) + \frac{M_{ex}}{n_r}$

end for

else

$M_{gex} = M_{gex} + M_{ex}$

end if

Transition $\mathbf{x}$ from an $\mathcal{I}$ state to $\mathcal{G}$ state

Set $M(\mathbf{x}, t) = 0$

end for

Let n_i be the number of cells in $\mathcal{I}$

for all cells $\mathbf{x} \in \mathcal{I}$ **do**

▷ Redistribute remaining excess mass evenly among interface cells

$M(\mathbf{x}, t) = M(\mathbf{x}, t) + \frac{M_{gex}}{n_i}$

end for

end procedure

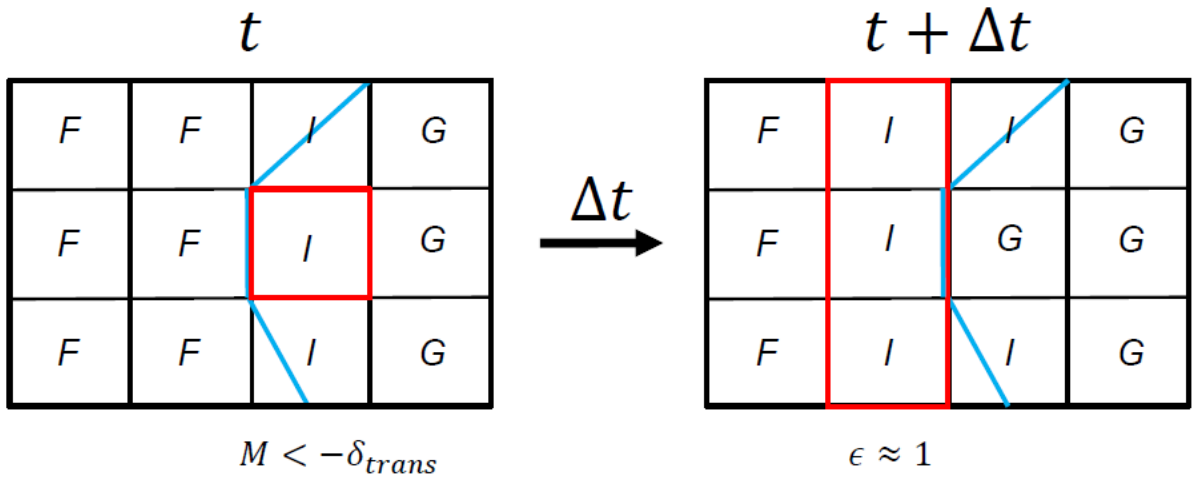

Figure 2.1: Example of cell state transitions. The interface cell highlighted in red on the left is transitioned to a gas cell as it has emptied. On the right, the three cells highlighted in red were transitioned from fluid to interface cells in order to keep the interface continuous.

Algorithm 1, as presented, ensures both mass conservation and continuity of the free-surface. Moreover, when mass redistribution inevitably occurs, it is first attempted to be redistributed and weighted in the direction in which the interface is propagating (e.g. line 1.45 or line 1.72. If there are no interface cells in the direction of interface propagation, it is instead redistributed to neighboring interface cells (e.g. line 1.50 or line 1.77). If there is no

neighboring cells which are interface cells, the excess mass is added onto the global excess mass, M_{gex}, which is eventually redistributed among all of the interface cells (e.g. line 1.87). The hierarchy of possible redistribution steps ensures that mass redistribution is done in the most physically meaningful way as is possible. Lastly, note that the interface normal, $\mathbf{n}$, is calculated using a finite difference approximation:

$$\mathbf{n}_{ij} = \frac{1}{2} \begin{Bmatrix} \epsilon_{i-1,j} - \epsilon_{i+1,j} \\ \epsilon_{i,j-1} - \epsilon_{i,j+1} \end{Bmatrix} \tag{2.2}$$

where i is the index of the node in the x-direction and j is the index of the node in the y-direction.

2.3.5 Boundary Conditions at the Free-Surface

Two important considerations not yet discussed are how boundary conditions are implemented at the interface in order to capture the interaction between the primary phase and the secondary phase, and how particle distributions that are missing from the streaming step are reconstructed. The degrees of freedom, f_i, are not tracked for gas cells. After the streaming step, interface cells will be missing particle distributions that would have streamed from gas cells–an issue that is depicted in Figure 2.2.

The missing particle distributions need to be reconstructed. Also, momentum needs to be conserved at the interface. When the particle distributions are reconstructed, they will be reconstructed in such a way that momentum is conserved between the primary fluid and the secondary fluid. In order to perform the reconstruction, there are a few assumptions that need to be made:

1. The velocity of the secondary fluid is equal to the velocity of the primary fluid at the free-surface, i.e. there is no-slip between the two-fluids.
2. The secondary fluid is at equilibrium and at constant pressure, p_G.
3. There is a force balance for opposite lattice directions.

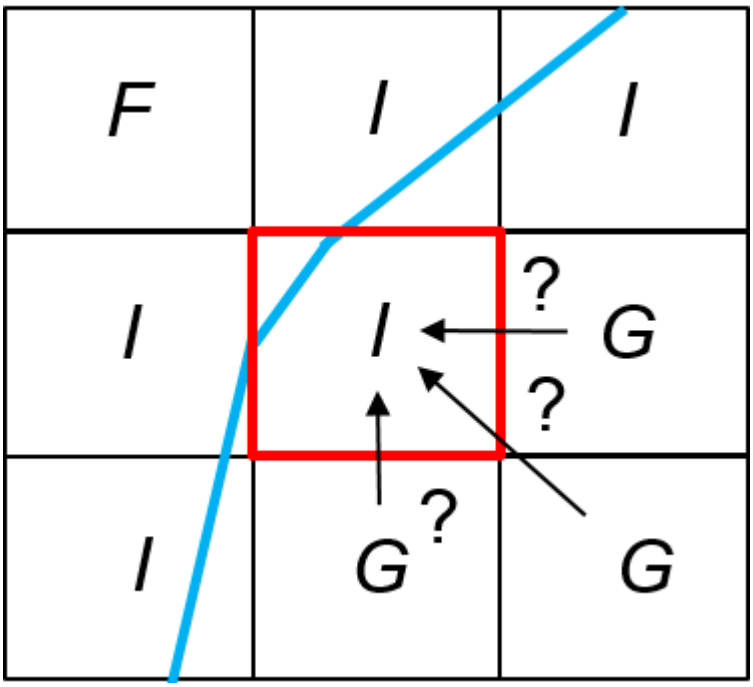

Figure 2.2: Example of a scenario in which particle distributions are missing post-streaming.

Because particle distributions are a measure of momentum transport, the pressure of the secondary fluid can be converted to the particle distribution scale and the missing particle distribution can be solved for algebraically. Consider Figure 2.3. Balancing the opposite lattice directions results in:

$$f_i + f_{\bar{ß}} = f_{\bar{ß}}^{eq}(\rho_G, \mathbf{u}) + f_i^{eq}(\rho_G, \mathbf{u}), \tag{2.3}$$

$$f_{\bar{ß}} = f_{\bar{ß}}^{eq}(\rho_G, \mathbf{u}) + f_i^{eq}(\rho_G, \mathbf{u}) - f_i. \tag{2.4}$$

Missing distribution functions can be reconstructed according to (2.4). In order for conservation of momentum to be satisfied along the free-surface, distribution functions coming from the direction of the interface normal, $\mathbf{n}$, must also be reconstructed. Thus, distribution functions are reconstructed if coming from a gas cell, or if $\mathbf{n} \cdot \boldsymbol{\xi}_{\bar{ß}} > 0$.

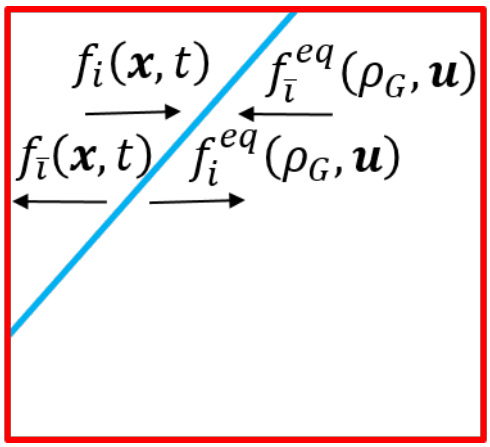

Figure 2.3: Particle distributions at free-surface for a pair of opposing lattice directions after gas pressure, ρ_G, is in the particle distribution form.

2.3.6 Resulting Algorithm for Simulating Free-Surface Flow using the Lattice Boltzmann Method

For clarity, the complete algorithm used in the current work for simulating free-surface flow using the Lattice Boltzmann Method is presented in Algorithm 2.

2.4 NUMERICAL STUDY OF PRIMARY CEMENTING

The free-surface LBM model was implemented and used to simulate primary cementing in a dry annulus, i.e. an annulus without drilling mud. The focus of the current study was the performance of different characteristic flow behaviors (as could potentially relate to different cement slurry mixes) when used to cement different imperfect wellbore geometries. Because the focus in regards to the wellbore is on geometrical imperfections, the entire wellbore annulus is not simulated, but instead a small section around a geometrical imperfection is considered. A schematic of an example primary cementing simulation, including boundary conditions, is shown in Figure 2.4.

Algorithm 2 Free-Surface Flow using the Lattice Boltzmann Method

procedure FREESURFACELBM(ρ_0, u_0, M_0, t_{max}) ▷ ρ_0, u_0, M_0 specify initial conditions

▷ Initialize data structures

Initialize $\rho(\mathbf{x}, 0)$ and $\mathbf{u}(\mathbf{x}, 0)$ to initial conditions

Initialize f to quasiequilibrium, $f_i(\mathbf{x}, 0) = f_i^{eq}(\rho(\mathbf{x}, 0), \mathbf{u}(\mathbf{x}, 0))$ (Equation (1.7))

▷ Main loop

for $t = 0 : \Delta t : t_{max}$ **do**

Mass transfer, $M(\mathbf{x}, t + \Delta t) = M(\mathbf{x}, t) + \sum_i \Delta M_i(\mathbf{x}, t)$, (Section 2.3.4.2)

▷ $\boldsymbol{\xi}_i$ depends on lattice

Stream particle distributions, $f_i(\mathbf{x} + \boldsymbol{\xi}_i \Delta t, t + \Delta t) = f_i(\mathbf{x}, t)$

Reconstruct particle distributions (Section 2.3.5)

Particle collisions (Section 1.3.2)

Enforce boundary conditions (Section 1.3.4)

Calculate macroscopic variables (Equation (1.4), Equation (1.5), Equation (1.6))

Update cell states (Algorithm 1)

end for

Post-process

end procedure

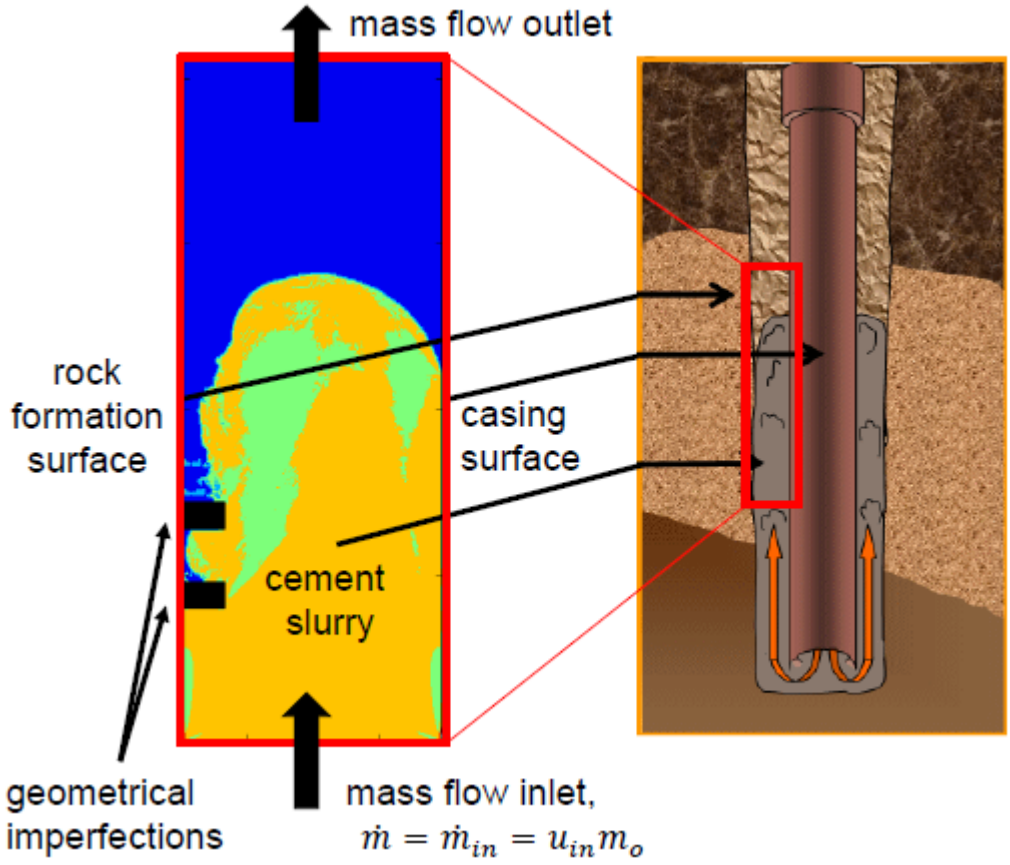

Figure 2.4: Example simulation used in primary cementing study. The black rectangles on the left boundary represent notches protruding from the rock formation surface. The contours are of the primary fluid (cement slurry) mass. The schematic on the right is courtesy of [1]

.

The simulations were carried out on a 50×500 lattice. For the mass inlet, a [38] velocity boundary condition was used in conjuction with a constant mass boundary condition, i.e. $M(\mathbf{x}_j, t) = M_0 = 1.0$ for all $\mathbf{x}_j$ along the inlet. This corresponded to a constant mass flow, $\dot{M}_{in} = M_0 u_0$, at inlet. For the outlet, mass was allowed to transfer out of the domain during the mass transfer step such that $f_{\bar{\beta}}(\mathbf{x} + \boldsymbol{\xi}_i \Delta t, t) = 0$ in (2.1) for all $\mathbf{x} + \boldsymbol{\xi}_i \Delta t$ that lie outside of the domain on the other side of the mass outlet (i.e. the boundary condition at the outlet is such that there is no backflow). All simulations were executed for 16000 time steps.

The different imperfect geometries that were considered at the rock formation surface were: flow over a cavity that is 30% of the annulus width, "cav 30×1"; flow over a cavity that is 60% of the annulus width, "cav 60×1"; flow over a square obstacle with sides that are 30% of the annulus width, "obs 30×1"; flow over two square obstacles with sides that are 30% of the annulus width, "obs 30×2"; flow over a square obstacle with sides that are 60% of the annulus width, "obs 60×1"; flow over two square obstacles with sides that are 60% of the annulus width, "obs 60×2"; and flow over a rectangular obstacle with width that is 60% of the annulus width and length that is four times the width, "obs $60 \times L$". The wellbore geometries that were considered herein are depicted in Figure 2.5.

In addition to wellbore geometry, different cement slurry material properties and cement slurry flow rates were considered, which are characterized by the dimensionless Reynold's number, $Re = \frac{\rho U L}{\mu_p}$, and Bingham number, $Bn = \frac{\tau_y L}{\mu_p U}$, of the flow, where $L \equiv$ the width of the annulus. A particular goal of the study was to investigate which Reynold's numbers and Bingham numbers were preferable for each geometry, and which Reynold's numbers and Bingham numbers performed well for all geometries. The dimensionless numbers were

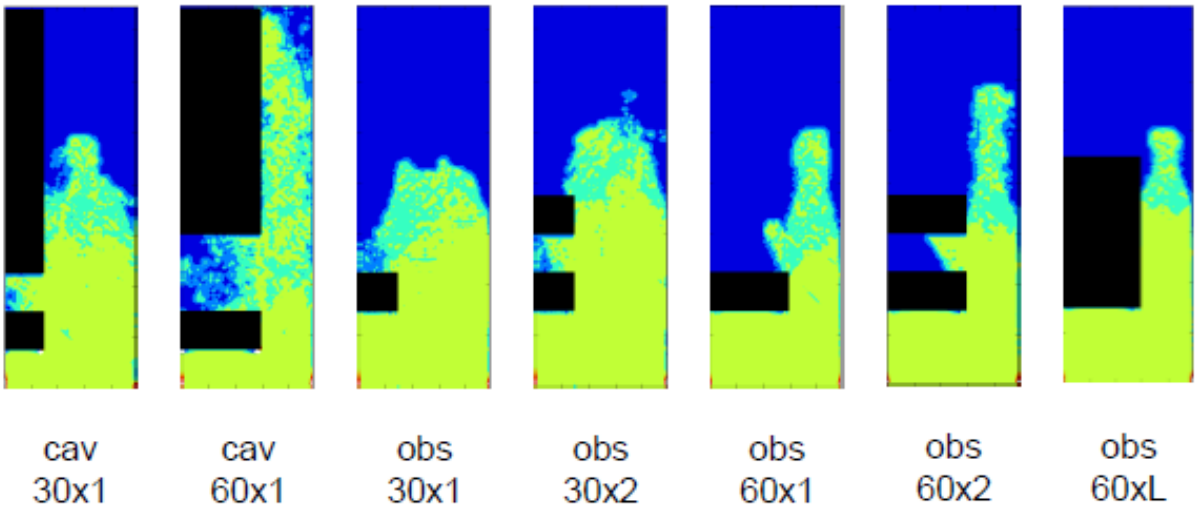

Figure 2.5: Wellbore geometries considered in the study.

defined as follows, $(Re, Bn) = (1.00, 4.00)$, $(2.50, 0.00)$, $(2.50, 1.00)$, $(2.50, 10.0)$, $(2.50, 25.0)$, $(5.00, 5.00)$, and $(12.5, 2.0)$. Figure 2.6 shows the percentage of the wellbore annulus section filled at the end of the cement simulation duration. The percent fill was calculated as:

$$\frac{\sum_{\mathbf{x}\in\mathcal{X}} \epsilon(\mathbf{x}, 16000)}{\sum_{\mathbf{x}\in\mathcal{X}} 1.0}. \tag{2.5}$$

Based upon Figure 2.6, some general statements can be made about what properties of the cement slurry flow are preferable. For example, low yield stress, and consquently low Bingham number flows ($Bn \leq 1.0$), approximately completely filled the annulus for every wellbore geometry considered. In addition, the negligible percentage of voids for the $(Re = 5.00, Bn = 5.00)$ and $(Re = 12.5, Bn = 2.0)$ slurry flows suggests that a if the ratio of Bn/Re is low, that the slurry flow will result in a low percentage of voids for cementing a dry hole as is desired. As Bn/Re increases, it appears that, in certain cases and wellbore geometries, the slurry flow tends to result in a larger percentage of voids (approximately 10%-40%). What is interesting to note is that for slurry flows that resulted in a percentage of

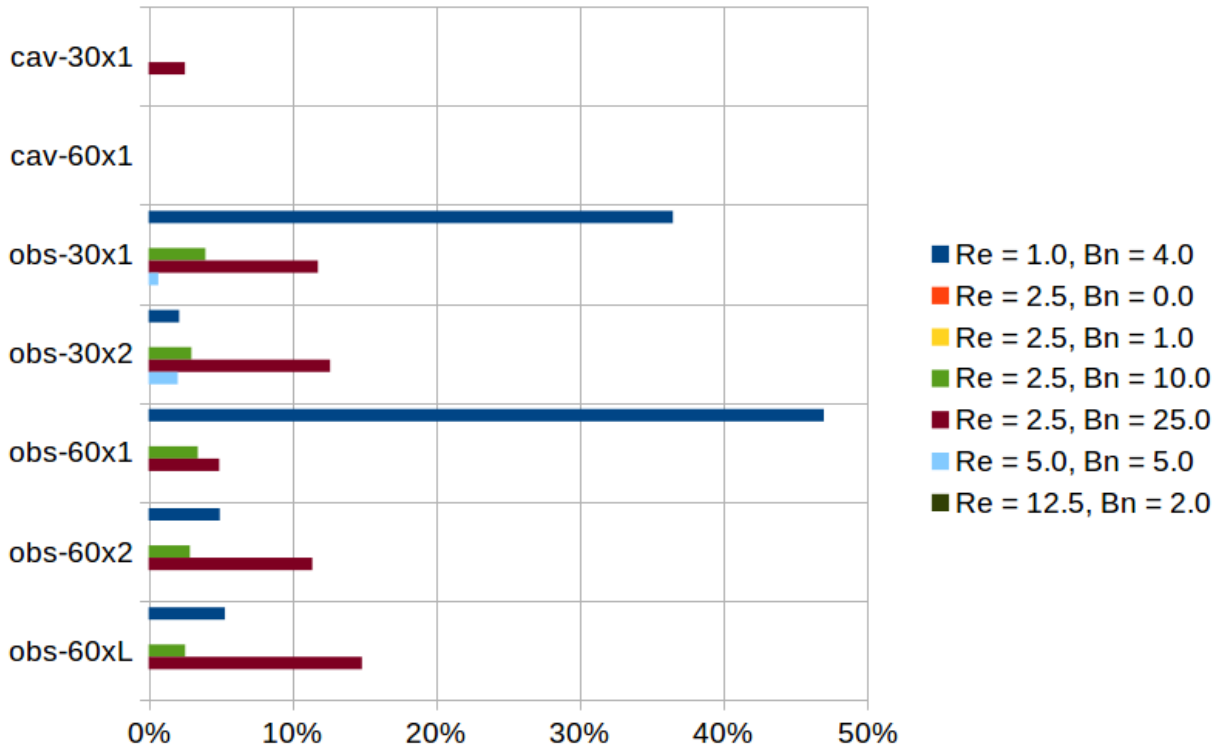

Figure 2.6: Percent of voids in wellbore at the end of simulation for each cement slurry flow through each wellbore geometry.

voids greater than 3%, there was a lack of consistency across wellbore geometries in terms of which slurry flow resulted in more voids and which slurry flow resulted in less, which suggests that generalities cannot always be made and that computational methods are necessary for understanding and designing slurry mixes for real-life wellbores.

2.5 CONCLUSIONS

An LBM model for simulating non-Newtonian and free-surface flow to represent cementing dry annuli in oil and gas wellbores was presented. The model was then used to study how different cement slurry flows, defined by different Reynold's numbers and Bingham numbers, would perform in different wellbore geometries. The results showed that in general, it is preferable that the yield stress and Bn/Re ratio of the slurry flow be low. However, beyond these considerations, it is not clear what slurry flow may be preferable for a given rock formation geometry. The results suggest that computational methods are necessary for (a) better understanding the mechanics of primary cementing and (b) for designing a cement mix for a given wellbore. The lattice Boltzmann method extended for simulating non-Newtonian and free-surface flow as presented in the current work has several properties that make it a good candidate for such a design framework:

- LBM is well-suited for simulating non-Newtonian fluids because the strain-rate tensor is computed local to each node and is second-order accurate [4, 39].
- LBM is well-suited for simulating multiphase multicomponent flow and free-surface flow because it can handle complicated interface shapes between fluid phases and components.
- LBM is easily written in parallel and as hardware architectures shifts sequential to parallel computing, it becomes increasingly important that code for simulating complex and computationally expensive phenomena be written in parallel.
- The LBM no-slip boundary condition works well with complex geometries, such as those that occur in realistic rock formation surfaces in drilled wellbores.

Future work would include developing a more physically realistic model. Primary cementing can involve multiple phases and multiple components, namely the cement slurry, a spacer fluid, and drilling mud. Possible future work would be make the model more general so as to be capable of simulating multiphase multicomponent flow. In addition, a more physically realistic model would simulate three-dimensional flow so as to be able to simulate eccentric annuli and three-dimensional rock formation imperfections.

3.0 CONCLUSIONS

Various Lattice Boltzmann methods were investigated for their efficacy in simulating primary cementing. Although non-Newtonian fluid mechanics only represent a portion of the challenges associated with simulating primary cementing, the fluid components that can be present in primary cementing exhibit various non-Newtonian behaviors such as yield stress or Bingham plastic behavior (e.g. cement slurry), power-law behavior (e.g. drilling mud), among other non-Newtonian behaviors. In Chapter 1, the accuracy, stability, and efficiency of Lattice Boltzmann models in simulating non-Newtonian fluid flow was investigated. Two different benchmark problems were chosen for the study: Poiseuille flow, and lid-driven square cavity flow, as Poiseuille flow is characterized by the development of velocity profiles and lid-driven cavity flow is characterized by the development of vortices. Conclusions from the study were presented in Section 1.5. In the context of studying the accuracy, stability, and efficiency of Lattice Boltzmann models for simulating non-Newtonian flow, future work would include investigating the effect of the choice of time step size and simulation Mach number (as in [66]) on the convergence rate and accuracy of the results and LB methods presented in Section 1.4. In addition, possible future work could include investigating other physical problems such as planar sudden expansion flow [5, 6, 8, 10], reentrant corner flow [22, 23], and flow around a cylinder [7]. In the context of simulating wellbore cementing, future work would include studying the accuracy, stability, and efficiency of Lattice Boltzmann models for simulating the thixotropic and time-dependent behavior of cement slurry [67].

In Chapter 2, the LBM algorithm for non-Newtonian flow is extended to simulate free surface flow. The extended LBM model is then used to study wellbore cementing. Future work for the wellbore cementing study would include developing a more physically realistic

model. Primary cementing can involve multiple phases and multiple components, namely the cement slurry, a spacer fluid, and drilling mud. Possible future work would be make the model more general so as to be capable of simulating multiphase multicomponent flow. In addition, a more physically realistic model would simulate three-dimensional flow so as to be able to simulate eccentric annuli and three-dimensional rock formation imperfections.

BIBLIOGRAPHY

[1] Introduction to cementing. http://www.drillingcourse.com/2015/12/introduction-to-cementing.html, 2015. Accessed: 2016-07-01.

[2] G Bohme. Non-newtonian fluid mechanics. series in applied mathematics and mechanics, 1987.

[3] Chen-Hao Wang and Jeng-Rong Ho. A lattice boltzmann approach for the non-newtonian effect in the blood flow. *Computers & Mathematics with Applications*, 62(1):75–86, 2011.

[4] T Krüger, F Varnik, and D Raabe. Second-order convergence of the deviatoric stress tensor in the standard bhatnagar-gross-krook lattice boltzmann method. *Physical Review E*, 82(2):025701, 2010.

[5] GH Tang, SB Wang, PX Ye, and WQ Tao. Bingham fluid simulation with the incompressible lattice boltzmann model. *Journal of Non-Newtonian Fluid Mechanics*, 166:145–151, 2011.

[6] Zhenhua Chai, Baochang Shi, Zhaoli Guo, and Fumei Rong. Multiple-relaxation-time lattice boltzmann model for generalized newtonian fluid flows. *Journal of Non-Newtonian Fluid Mechanics*, 166(5):332–342, 2011.

[7] Keivan Fallah, Morteza Khayat, Mohammad Hossein Borghei, Atena Ghaderi, and Ehsan Fattahi. Multiple-relaxation-time lattice boltzmann simulation of non-newtonian flows past a rotating circular cylinder. *Journal of Non-Newtonian Fluid Mechanics*, 177:1–14, 2012.

[8] SongGui Chen, QiCheng Sun, Feng Jin, and JianGuo Liu. Simulations of bingham plastic flows with the multiple-relaxation-time lattice boltzmann model. *Science China Physics, Mechanics and Astronomy*, 57:532–540, 2014.

[9] A Vikhansky. Lattice-boltzmann method for yield-stress liquids. *Journal of Non-Newtonian Fluid Mechanics*, 155:95–100, 2008.

[10] Chen-Hao Wang and Jeng-Rong Ho. Lattice boltzmann modeling of bingham plastics. *Physica A: Statistical Mechanics and its Applications*, 387:4740–4748, 2008.

[11] Liang Wang, Jianchun Mi, Xuhui Meng, and Zhaoli Guo. A localized mass-conserving lattice boltzmann approach for non-newtonian fluid flows. *Communications in Computational Physics*, 17(04):908–924, 2015.

[12] J Boyd, James Buick, and S Green. A second-order accurate lattice boltzmann non-newtonian flow model. *Journal of physics A: Mathematical and General*, 39:14241–14247, 2006.

[13] Mahmud Ashrafizaadeh and Hani Bakhshaei. A comparison of non-newtonian models for lattice boltzmann blood flow simulations. *Computers & Mathematics with Applications*, 58(5):1045–1054, 2009.

[14] James D Sterling and Shiyi Chen. Stability analysis of lattice boltzmann methods. *arXiv preprint comp-gas/9306001*, 1993.

[15] James D Sterling and Shiyi Chen. Stability analysis of lattice boltzmann methods. *Journal of Computational Physics*, 123(1):196–206, 1996.

[16] Saleh Bawazeer. Stability and accuracy of lattice boltzmann method. 2013.

[17] Pierre Lallemand and Li-Shi Luo. Theory of the lattice boltzmann method: Dispersion, dissipation, isotropy, galilean invariance, and stability. *Physical Review E*, 61:6546–6542, 2000.

[18] Oldřich Švec, Jan Skoček, Henrik Stang, John Forbes Olesen, and Peter Noe Poulsen. Flow simulation of fiber reinforced self compacting concrete using lattice boltzmann method. 2011.

[19] Oldřich Švec, Jan Skoček, Henrik Stang, Mette R Geiker, and Nicolas Roussel. Free surface flow of a suspension of rigid particles in a non-newtonian fluid: A lattice boltzmann approach. *Journal of Non-Newtonian Fluid Mechanics*, 179:32–42, 2012.

[20] Yanlong Zhao, Zhiming Wang, Quanshu Zeng, Jiangtao Li, and Xiao Guo. Lattice boltzmann simulation for steady displacement interface in cementing horizontal wells with eccentric annuli. *Journal of Petroleum Science and Engineering*, 145:213–221, 2016.

[21] Jonas Latt. *Hydrodynamic limit of lattice Boltzmann equations*. PhD thesis, University of Geneva, 2007.

[22] Susana Gabbanelli, German Drazer, and Joel Koplik. Lattice boltzmann method for non-newtonian (power-law) fluids. *Physical Review E*, 72(4):046312, 2005.

[23] M Yoshino, Y Hotta, T Hirozane, and M Endo. A numerical method for incompressible non-newtonian fluid flows based on the lattice boltzmann method. *Journal of non-newtonian fluid mechanics*, 147:69–78, 2007.

[24] Dominique d'Humieres. Generalized lattice-boltzmann equations. *Rarefied gas dynamics- Theory and simulations*, pages 450–458, 1994.

[25] RA Brownlee, Alexander N Gorban, and Jeremy Levesley. Stabilization of the lattice boltzmann method using the ehrenfests' coarse-graining idea. *Physical Review E*, 74(3):037703, 2006.

[26] RA Brownlee, Alexander N Gorban, and Jeremy Levesley. Stability and stabilization of the lattice boltzmann method. *Physical Review E*, 75(3):036711, 2007.

[27] RA Brownlee, Alexander N Gorban, and Jeremy Levesley. Nonequilibrium entropy limiters in lattice boltzmann methods. *Physica A: Statistical Mechanics and its Applications*, 387(2):385–406, 2008.

[28] Dave Packwood. Entropy balance and dispersive oscillations in lattice boltzmann models. *Physical Review E*, 80(6):067701, 2009.

[29] Alexander N Gorban and DAVID J Packwood. Enhancement of the stability of lattice boltzmann methods by dissipation control. *Physica A: Statistical Mechanics and its Applications*, 414:285–299, 2014.

[30] Shiyi Chen and Gary D Doolen. Lattice boltzmann method for fluid flows. *Annual review of fluid mechanics*, 30:329–364, 1998.

[31] Sauro Succi. *The Lattice Boltzmann Equation for Fluid Dynamics and Beyond*. Oxford University Press, New York, 2001.

[32] Carlo Cercignani. *Mathematical methods in kinetic theory*. Springer, 1990.

[33] P. Bhatnagar, E. Gross, and M. Krook. A model for collisional processes in gases i: small amplitude processes in charged and neutral one-component system. *Phys. Rev.*, 94, 1954.

[34] Dieter A Wolf-Gladrow. *Lattice-gas cellular automata and lattice Boltzmann models: An Introduction*. Springer Science & Business Media, 2000.

[35] Paul J Dellar. Incompressible limits of lattice boltzmann equations using multiple relaxation times. *Journal of Computational Physics*, 190(2):351–370, 2003.

[36] Dominique d'Humières. Multiple–relaxation–time lattice boltzmann models in three dimensions. *Philosophical Transactions of the Royal Society of London A: Mathematical, Physical and Engineering Sciences*, 360(1792):437–451, 2002.

[37] Matthew Grasinger, Zichang Li, Alex Vuotto, John Brigham, Anthony Iannacchione, Julie Vandenbossche, et al. Simulation of cement slurry flow to assess the potential for voids and channels in wellbore cementing processes. In *SPE Eastern Regional Meeting*. Society of Petroleum Engineers, 2015.

[38] Qisu Zou and Xiaoyi He. On pressure and velocity boundary conditions for the lattice boltzmann bgk model. *Physics of Fluids (1994-present)*, 9:1591–1598, 1997.

[39] Timm Krüger, Fathollah Varnik, and Dierk Raabe. Shear stress in lattice boltzmann simulations. *Physical Review E*, 79:046704, 2009.

[40] Eugene Cook Bingham. *Fluidity and plasticity*, volume 2. McGraw-Hill Book Compny, Incorporated, 1922.

[41] Tasos C Papanastasiou. Flows of materials with yield. *Journal of Rheology (1978-present)*, 31:385–404, 1987.

[42] Qiuxiang Li, Ning Hong, Baochang Shi, and Zhenhua Chai. Simulation of power-law fluid flows in two-dimensional square cavity using multi-relaxation-time lattice boltzmann method. *Communications in Computational Physics*, 15(01):265–284, 2014.

[43] Alexandros Syrakos, Georgios C Georgiou, and Andreas N Alexandrou. Performance of the finite volume method in solving regularised bingham flows: Inertia effects in the lid-driven cavity flow. *Journal of Non-Newtonian Fluid Mechanics*, 208:88–107, 2014.

[44] Michael J Economides. 1 implications of cementing on well performance. *Developments in Petroleum Science*, 28:1–6, 1990.

[45] PB Jackson, CE Murphey, et al. Effect of casing pressure on gas flow through a sheath of set cement. In *SPE/IADC drilling conference*. Society of Petroleum Engineers, 1993.

[46] KJ Goodwin, RJ Crook, et al. Cement sheath stress failure. *SPE Drilling Engineering*, 7(04):291–296, 1992.

[47] Maurice B Dusseault, Richard E Jackson, and Daniel Macdonald. Towards a road map for mitigating the rates and occurrences of long-term wellbore leakage. *University of Waterloo and Geofirma Engineering LTD*, 2014.

[48] Zichang Li, Julie Vandenbossche, Anthony Iannacchione, John Brigham, Barbara Kutchko, et al. Theory-based review of limitations with static gel strength in cement/matrix characterization. *SPE Drilling & Completion*, 2016.

[49] SH Bittleston, J Ferguson, and IA Frigaard. Mud removal and cement placement during primary cementing of an oil well–laminar non-newtonian displacements in an eccentric annular hele-shaw cell. *Journal of Engineering Mathematics*, 2:229–253, 2002.

[50] PR Cheung and Robert M Beirute. Gas flow in cements. *Journal of petroleum technology*, 06:1041–1048, 1985.

[51] Dennis C Levine, Eugene W Thomas, HP Bezner, and Glen C Tolle. Annular gas flow after cementing: a look at practical solutions. Society of Petroleum Engineers, 1979.

[52] RB Stewart and Schouten FC. Gas invasion and migration in cemented annuli: Causes and cures. *SPE drilling engineering*, 01:77–82, 1988.

[53] Soran Talabani, GA Chukwu, and DG Hatzignatiou. A unique experimental study reveals how to prevent gas migration in a cemented annulus. Society of Petroleum Engineers, 1993.

[54] Muhammad Zulqarnain. Simulations of the primary cement placement in annular geometries during well completion using computational fluid dynamics (cfd). Technical report, Baton Rouge, 2012.

[55] Robert M Beirute and Raymond W Flumerfelt. Mechanics of the displacement process of drilling muds by cement slurries using an accurate rheological model. Society of Petroleum Engineers, 1977.

[56] Daniel T Thorne and C Michael. *Lattice Boltzmann modeling: An introduction for geoscientists and engineers*. Springer, 2006.

[57] C Ferraris, F De Larrard, and N Martys. Fresh concrete rheology: recent developments. *Materials Science of Concrete VI, Amer. Cer. Soc. Ed. S. Mindess, J. Skalny*, pages 215–241, 2001.

[58] Chiara F Ferraris and François de Larrard. *Testing and modelling of fresh concrete rheology*. US Department of Commerce, Technology Administration, National Institute of Standards and Technology, 1998.

[59] Geoffrey Howarth Tattersall. *Workability and quality control of concrete*. CRC Press, 2003.

[60] Nicolas Roussel, Mette R Geiker, Frédéric Dufour, Lars N Thrane, and Peter Szabo. Computational modeling of concrete flow: General overview. *Cement and Concrete research*, 37:1298–1307, 2007.

[61] Nicolas Roussel, Annika Gram, Massimiliano Cremonesi, Liberato Ferrara, Knut Krenzer, Viktor Mechtcherine, Sergiy Shyshko, Jan Skocec, Jon Spangenberg, Oldrich Svec, et al. Numerical simulations of concrete flow: A benchmark comparison. *Cement and Concrete Research*, 2015.

[62] Zhenhua Chai, Baochang Shi, Zhaoli Guo, and Fumei Rong. Multiple-relaxation-time lattice boltzmann model for generalized newtonian fluid flows. *Journal of Non-Newtonian Fluid Mechanics*, 5:332–342, 2011.

[63] Timothy Nigel Phillips and Gareth Wyn Roberts. Lattice boltzmann models for non-newtonian flows. *IMA journal of applied mathematics*, 76(5):790–816, 2011.

[64] Carolin Körner, Michael Thies, Torsten Hofmann, Nils Thürey, and Ulrich Rüde. Lattice boltzmann model for free surface flow for modeling foaming. *Journal of Statistical Physics*, 121:179–196, 2005.

[65] Nils Thürey, C Körner, and U Rüde. Interactive free surface fluids with the lattice boltzmann method. *Technical Report05-4. University of Erlangen-Nuremberg, Germany*, 2005.

[66] Daniel Conrad, Andreas Schneider, and Martin Böhle. Accuracy of non-newtonian lattice boltzmann simulations. *Journal of Computational Physics*, 301:218–229, 2015.

[67] Nicolas Roussel. Steady and transient flow behaviour of fresh cement pastes. *Cement and concrete research*, 35:1656–1664, 2005.